1 OF 1
AD A
080309

END
DATE
FILMED
3–80
DDC

AFOSR-TR- 79-1329 ②LEVEL II

CHARACTERISTICS OF PLASMA-BEAM WALL
INTERACTIONS

TABLE OF CONTENTS

80 1 29 056

CHARACTERISTICS OF PLASMA-BEAM

WALL INTERACTIONS

General Remarks

The present report covers work performed under Grant AFOSR-78-3603 concerning a series of investigations related to high-density plasma beams.

The general purpose of the work was aimed at understanding the physical characteristics of the beam in order to use the beam in several applications of great interest to the Air Force. Most of these required the formation and injection of dense, highly ionized plasmas in magnetic "compression" machines. These machines then yield according to the extent of compression used X-rays or neutrons fluxes or both.

The production of hot plasmas of high density, of course, has been known for several years following the classic work on the plasma focus. The ability to produce hot plasma beams of very high density, however, is not readily found, specially if one requires the beam to be well collimated, dynamically stable and with densities better than $10^{17}/cm^3$.

The work described here, substantially summarizes the effort of several years. It is felt that the state of the art in the design of plasma guns of the Cheng type is finally understood. We are also convinced that because of this understanding one can construct a

ii

group of guns to be operated collectively for the purpose of injecting

plasmas of several configurations and this with a high degree of

reliability.

The work described in the report includes the contribution of

several investigators in particular Dr. A. Ferendeci and Mr. R. Mesli

and to a lesser extent J. Kasky and R. Webster.

Part of these investigations have been reported at the 1979 IEEE

Conference on Plasma Science, Montreal, Canada (Papers IB 11). A series

of papers are presently being proposed for submission to various

Scientific Journals.

iii

CHAPTER I

INTRODUCTION

The Shiva machine is a plasma device used to generate intense
X-rays[1] by compressing a plasma shell by the magnetic self field of
a current passing through the shell.

The technique originally used to produce the plasma shell was
to implode a thin cylindrical Aℓ foil[2,3] in the implosion chamber by
discharging a high energy capacitor bank. In this way, the tempera-
ture density and stability requirements of the Shiva machine were
fulfilled. One of the experimental difficulties was that the implo-
sion chamber had to be replaced after each shot because of mechanical
and radiation damage.

To avoid the difficulty described above, an alternative techni-
que was suggested to replace the Aℓ foil by a cylindrical puff of
gas.[4] The gas was injected into the implosion chamber through cir-
cular openings in one of the electrodes. A cylindrical plasma shell
is then formed by discharging the condenser bank across the chamber.
The concept of substituting a gas shell in place of the liner foil
offers definitive advantages. In Ref. 4, extensive investigations
have been carried out towards the understanding of the dynamics of
the puffed gas mode. However, the experimental results from this
technique indicated a non-uniform density distribution of the gas
shell both in the axial and azimuthal directions.

A second alternative approach to substitute the liner foil in
the Shiva implosion chamber by a plasma shell rather than an unionized
gas shell was proposed a few years ago by M. Wolfe.[5] The plasma,
which has to be produced initially by a coaxial gun, is then injected
into the implosion chamber through circular holes. Hopefully, a
cylindrical uniform plasma shell will be formed between the plates
of the chamber which will consequently be imploded by the capacitor
bank. From the requirements of the Shiva machine 100 μ gm of plasma
is needed to be injected into the implosion chamber. This is accom-
plished through 90 holes, each having a diameter of 1 cm and aligned
around a circle having 20 cm radius. The corresponding minimum number
densities for different gases satisfying the Shiva criteria were
found to be:[6]

Hydrogen	$4.23 \times 10^{17} \text{ cm}^{-3}$
Helium	$1.06 \times 10^{17} \text{ cm}^{-3}$
Aluminum	$1.57 \times 10^{16} \text{ cm}^{-3}$
Copper	$6.66 \times 10^{15} \text{ cm}^{-3}$

TABLE 1.1

The separation between the plates of the implosion chamber is 2 cm,
therefore the uniformity of the injected plasma in both the axial
and azimuthal directions are of great importance. Also, during the
injection period there should be very small recombination of the

injected plasma such that the required mass density can be maintained.

In summary, then, the idea of the plasma injection into the Shiva machine consisted of producing a symmetric, highly dense and energetic cylindrical plasma shell from a subsidiary gun[7,8] and of directing this plasma into the Shiva implosion chamber. Theory predicts that any initial fluting in the plasma will damp out during the implosion.[7]

The work described in this dissertation was for the purpose of testing this concept. A plasma beam produced by a small scale co-axial gun, was to be injected through a hole drilled in the center of a plate. A second solid plate placed 2 cm away from the first one simulated the unperforated electrode of the implosion chamber. In this study, special attention was to be directed to the production of an efficient injection scheme and to the understanding of the dynamics of the plasma flowing through openings in a plate.

The incident plasma beam is produced by an improved coaxial Cheng gun.[9] Various diagnostic techniques are reported here later to study the behavior and the dynamics of the plasma beam before and after passing through the hole. The spatial distribution of the injected plasma in both axial and azimuthal directions was measured.

The important parameters that have been determined were: the temperature, density and directed velocity of the plasma beam. The diverging flow of the jet as it comes out of the plate has been observed. Electron density measurements were initially made by means

of laser interferometry. These measurements were checked by optical
spectroscopy which also yielded the temperature. High speed photo-
graphic techniques gave velocity measurements and aided in the obser-
vation of the plasma behavior. The formation of the plasma beam was
monitored by the time dependent voltage and current characteristics
of the discharge mechanism.

Concurrently, theoretical work using a single fluid model was
undertaken in an attempt to analyze the flow pattern of the jet as
it escaped into the implosion chamber. This is given in details in
Chapter 2.

A description of the experimental layout and the diagnostic
techniques used to perform the measurements mentioned above is out-
lined in Chapter 3.

In the fourth chapter the experimental results of the observa-
tions made are discussed.

Finally, in the fifth chapter the theory is compared with the
experimental observations and suggestions for further study are made.

CHAPTER II

THEORETICAL CONSIDERATIONS

2.1 Formulation of the Problem

The theoretical discussion in this chapter deals with the
dynamics of the plasma injection mechanism into the Shiva implosion
chamber.

To understand the justification of the assumptions underlying
the equations of motion for the plasma, a few comments on the construc-
tion of the implosion chamber are in place.

The device consists of two parallel electrodes (Fig. 2.1), one
of which is perforated to allow the injection of the plasma. The
condenser bank used in conjunction with the Shiva machine is allowed
to discharge shortly after the injection has taken place. At that
instant the plasma is concentrated mainly in the vicinity of the entry
holes. The arc discharge will be initiated at the place of minimum
inductance in the plasma that is providing a galvanic conduction path
for the current.

Therefore, the conditions to be investigated will correspond to
the behavior of the injected plasma in the vicinity of the holes.
This can be approximated quite reasonably by a steady flow of the
plasma as it passes through the hole. Indeed, one notices that the
transit time of the plasma through the thickness of the plate is very
short compared to the lifetime of the plasma beam incident on the
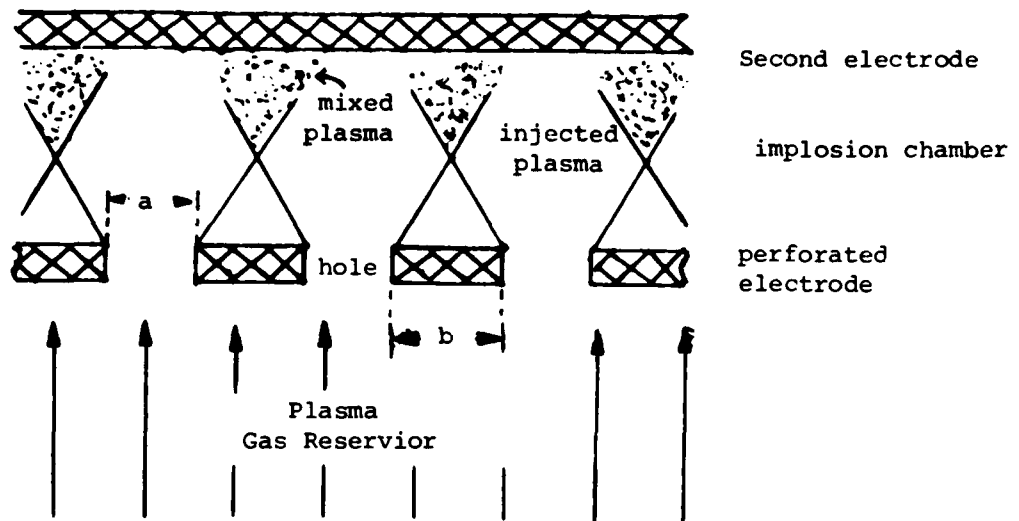plate.

Figure 2.1.   Schematic representation of the idealized

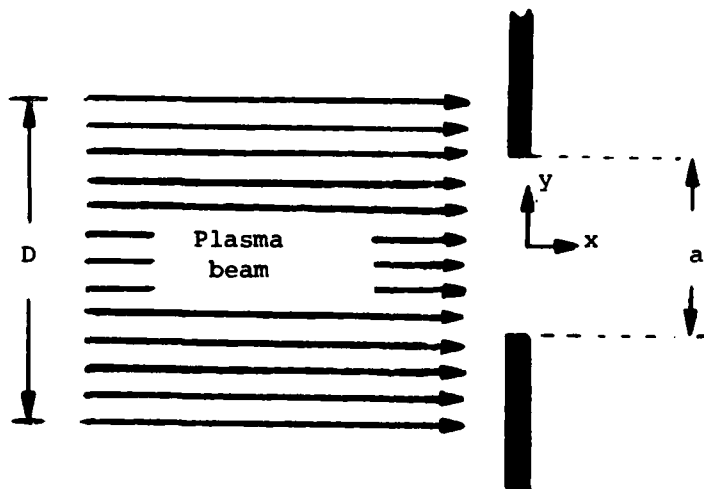geometry for the plasma injection.

Figure 2.2.   Theoretical model of the beam single hole

interaction.

Because the arc discharge occurs very soon after the incidence of the plasma in the chamber and before the flow is appreciably altered by the back electrode, we can neglect the effect of this plate on the flow pattern of the jet.

The model used to study the injection mechanism assumes thus that a steady state He plasma beam is incident on a plate placed perpendicular to the axis of the beam. The plate has a single infinite slit of width a as shown in Fig. 2.2. The slit width is assumed to be smaller than the diameter of the beam D. We assume that the results obtained for a single slit can be generalized to the multiple holes of the Shiva machine.

Earlier experimental results on the plasma beam showed that the beam is radially uniform, very dense and that it propagates with supersonic speeds.[10,11] Observations have also shown that the jet possesses an irrotational motion and can be considered a compressible fluid. As a first approximation, a single fluid model is chosen for the plasma by assuming a small value of Debye Length. The molecular effects on the plasma, i.e., recombination, viscosity, heat conduction and heat transfer are neglected. Formation of shocks are excluded in this model. Magnetic forces are excluded by assuming that there are no trapped fields in the plasma and that no currents flow between the gun and the perforated plate.

The validity of these assumptions have been verified by the experimental results obtained through the measurements.

A two dimensional model is considered as shown in Fig. 2.2. The x-axis is taken to be along the axis of the flow and the y-axis perpendicular to it. The width of the slit in the z direction is assumed infinite.

Most of the work found in the literature, on the theory of supersonic gas flow from an orifice has dealt with neutral compres- ble gases flowing through holes and nozzles. In most of the cases discussed, the back pressure is comparable to that of the incident pressure of the gas.[12,13] In the present work, the ratio of the exit to the back pressure of the outer medium is very high since the jet flows into a high vacuum. The plasma flow is still expected to form a diverging jet structure.

2.2 Governing Equations

Using the above assumptions, the governing equations for the escaping jet are deduced from the general magnetohydrodynamic equations and are[14,15]

$$\rho\,(\vec{V}\cdot\nabla)\vec{V} + \nabla p = 0 \tag{2.1}$$

$$\nabla\cdot(\rho\vec{V}) = 0 \tag{2.2}$$

$$\frac{dp}{d\rho} = \gamma\,\frac{p}{\rho} = c^2 \tag{2.3}$$

$$\nabla\times\vec{V} = 0 \tag{2.4}$$

$$ds = C_V\,\frac{dp}{p} - C_p\,\frac{d\rho}{\rho} \tag{2.5}$$

where ρ = mass density = nm

$\vec{V}$ = fluid velocity vector = average flow velocity

$$p = \text{kinetic pressure} = n\,k\,T$$

$$\gamma = \text{ratio of specific heats} = C_p/C_v$$

$$C = \text{speed of sound} = (\gamma\,kT/m)^{1/2}$$

$$s = \text{entropy}$$

The five equations (2.1) to (2.5) express respectively conservation of momentum, conservation of mass, the equation of state, the condition for irrotational flow and the equation of state for an ideal gas flow.

Combining equations (2.1), (2.3) and (2.5) into equation (2.2), the governing equations of a supersonic steady continuous homoenergetic and irrotational flow of an ideal gas with constant specific heats reduce to[15]

$$\nabla \cdot \vec{V} = \frac{1}{C^2}\,\vec{V} \cdot \nabla\left(\frac{V^2}{2}\right) \tag{2.6}$$

$$\nabla \times \vec{V} = 0 \tag{2.4}$$

For a cartesian system, equations (2.4) and (2.6) become

$$\left(1 - \frac{u^2}{C^2}\right)\frac{\partial u}{\partial x} - \frac{uv}{C^2}\frac{\partial u}{\partial y} - \frac{uv}{C^2}\frac{\partial u}{\partial x} + \left(1 - \frac{v^2}{C^2}\right)\frac{\partial v}{\partial y} = 0 \tag{2.7}$$

$$\frac{\partial v}{\partial x} - \frac{\partial u}{\partial y} = 0 \tag{2.8}$$

where u and v denote the components of the flow velocity $\vec{V}$ in the x and y directions, respectively.

2.3 Method of Characteristics

Expressions (2.7) and (2.8) form a set of non-linear partial differential equations of the hyperbolic type. The system of equations

is solved by the well known numerical method of characteristics. Ref. 15,16,17,18,19 and 20 deal extensively with the method of characteristics.

The solutions of equations (2.7) and (2.8) represent the slope of the physical characteristics (Mach waves) at each point of the flow and are given in Ref. 15 as:

$$C_+: \quad \frac{dy}{dx} = \frac{-\frac{uv}{c^2} - \sqrt{\frac{u^2 + v^2}{c^2} - 1}}{1 - \frac{u^2}{c^2}} \tag{2.9}$$

$$C_-: \quad \frac{dy}{dx} = \frac{-\frac{uv}{c^2} + \sqrt{\frac{u^2 + v^2}{c^2} - 1}}{1 - \frac{u^2}{c^2}} \tag{2.10}$$

Making use of the relationship between the magnitude of the velocity V and its components u and v and the flow angle θ (see Fig. 2.3) as well as the relationship between the Mach angle α and the Mach number M (see Fig. 2.4), an alternate form of expressions (2.9) and (2.10) can be written as

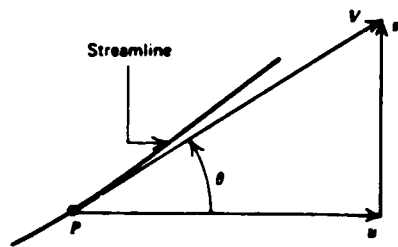$$C_+: \quad \frac{dy}{dx} = \tan(\theta + \alpha) \tag{2.11}$$

$$C_-: \quad \frac{dy}{dx} = \tan(\theta - \alpha) \tag{2.12}$$

TABLE 2.1

| State	$\theta_*^-(0)$	$\theta_*^+(0)$	$\theta(0)$	$\nu(M)$	M	$\mu(0)$	$\theta+\alpha(0)$	$\theta-\alpha(0)$	T/T_t	ρ/ρ_t
1	21.787	-21.787	0	21.787	2.00	30.00	30.00	-30.00	.4286	.2806
2	31.880	-21.787	5.0500	26.832	2.25	26.39	31.44	-21.34	.3721	.2270
3	40.900	-21.787	9.5600	31.345	2.50	23.58	33.14	-14.02	.3243	.1847
4	48.940	-21.787	13.580	35.364	2.75	21.32	34.90	-7.74	.2840	.1514
5	56.100	-21.787	17.160	38.942	3.00	19.47	36.63	-2.31	.2500	.1250
6	68.200	-21.787	23.200	44.988	3.50	16.60	39.80	6.60	.1967	$.8725 \times 10^{-1}$
7	31.880	-31.880	0	31.880	2.53	23.28	31.88	-31.88	.3191	.1803
8	40.900	-31.880	4.600	36.390	2.82	20.77	25.37	-16.17	.2739	.1434
9	48.940	-31.880	8.5300	40.410	3.11	18.76	27.29	-10.23	.2367	.1152
10	56.100	-31.880	12.110	43.990	3.41	17.05	29.16	-4.94	.2051	$.3288 \times 10^{-1}$
11	40.900	-40.900	0	40.900	3.15	18.51	18.51	-18.51	.2322	.1119
12	77.920	-21.787	28.067	49.854	4.00	14.48	42.55	13.59	.1579	$.6275 \times 10^{-1}$
13	87.540	-21.787	32.870	54.670	4.62	12.50	45.37	20.37	.1232	$.4326 \times 10^{-1}$
14	100.408	-21.787	39.300	61.108	5.75	10.02	49.32	29.28	$.8319 \times 10^{-1}$	$.2399 \times 10^{-1}$
15	48.387	-21.787	48.290	0.097	8.50	6.750	55.04	41.54	$.3987 \times 10^{-1}$	$.7960 \times 10^{-2}$
16	158.210	-21.787	68.210	→ 90	→ ∞	→ 0	68.21	68.21	→ 0	→ 0

$$\theta_*^+ = \theta - \nu(M)$$
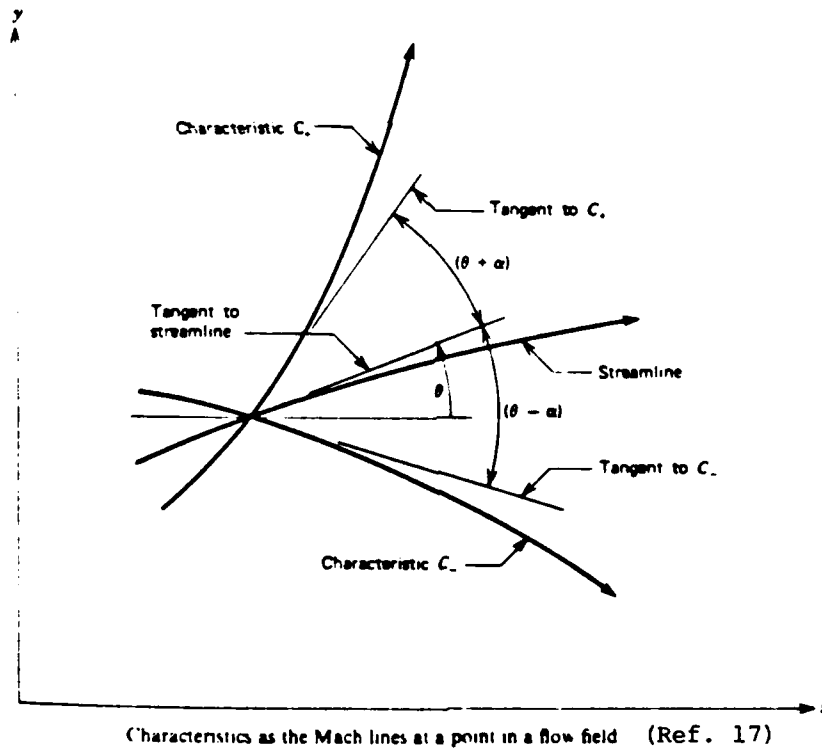$$\theta_*^- = \theta + \nu(M)$$

Relationship between the velocity components u and v, and the velocity magnitude V and the flow angle θ. (Ref. 17)
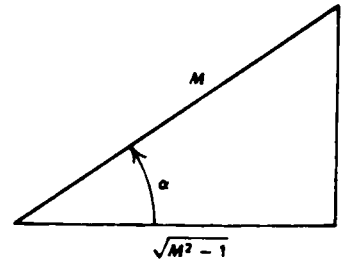
Figure 2.3

Relationship between the Mach angle α and the Mach number M. (Ref. 17)

Figure 2.4

Characteristics as the Mach lines at a point in a flow field (Ref. 17)

Figure 2.5

Here the flow angle θ is defined as

$$\theta = \tan^{-} \left(\frac{u}{v}\right) \qquad (2.13)$$

and the Mach angle α as

$$\alpha = \sin^{-1} \frac{C}{V} = \sin^{-1} \frac{1}{M} \qquad (2.14)$$

where the Mach number M is defined in the usual manner as

$$M \equiv \frac{V}{C} \qquad (2.15)$$

The characteristics C_+ and C_- as the Mach lines at a point in a flow field are shown in Fig. 2.5.

The equations relating the changes in direction of flow measured by θ and the resulting change in the magnitude of the gas velocity V across Mach waves provide a workable expression for the numerical method of characteristics. These can be written as[16,17]:

$$d\theta = \pm \frac{\sqrt{M^2 - 1}}{M(1 + \frac{\gamma-1}{2} M^2)} dM \qquad (2.16)$$

The positive and negative forms of equation (2.16) refer to the crossing of a Mach wave whose slopes are $(dy/dx) = \tan(\theta - \alpha)$ and $(dy/dx) = \tan(\theta + \alpha)$, respectively. The familiar form of equation (2.16) is

$$d\theta = \pm d\nu \qquad (2.17)$$

For a perfect gas, the integrated form of (2.17) is written as:

$$\nu(M) = \sqrt{\frac{\gamma + 1}{\gamma - 1}} \; \tan^{-1} \sqrt{\frac{\gamma - 1}{\gamma + 1}(M^2 - 1)} - \tan^{-1}(M^2 - 1) \quad (2.18)$$

$\nu(M)$ is called the Prandtl Meyer angle and is defined[21] as the angle through which the stream flow turns in expanding from a Mach number of 1 to a supersonic Mach number M. Equation 2.17 is the main expression for the step by step numerical integration procedure used in the method of characteristics.

A complete set of tables, equations, and figures to be used in the analysis of Helium gas flowing at supersonic and hypersonic speeds are given in Ref. 21.

2.4 Application for a Flow with M = 2

The flow in the vicinity of the opening is obtained as stated in section 2.1, by neglecting the presence of the second plate. From the experimental results, the incident plasma beam, before it reaches the perforated plate has a Mach number approximately 2. Therefore, the method of characteristics have been applied for the case of an initial Mach number $M = 2$. From symmetry considerations, calculations have been carried out only for the upper half of the flow field. The corresponding computations are given in Table 2.1. The notation θ_* used is defined[15] as the flow angle corresponding to M = 1. Since for M = 1 the value of ν becomes zero, the integration of equation (2.15) gives the following expressions:

TABLE 2.1

State	$\theta_*^-{}^{(0)}$	$\theta_*^+{}^{(0)}$	$\theta^{(0)}$	$\nu(M)$	M	$\mu^{(0)}$	$\theta+\alpha^{(0)}$	$\theta-\alpha^{(0)}$	T/T_t	$\rho/\rho t$
1	21.78?	-21.787	0	21.787	2.00	30.00	30.00	-30.00	.4286	.2806
2	31.880	-21.787	5.0500	26.832	2.25	26.39	31.44	-21.34	.3721	.2270
3	40.900	-21.787	9.5600	31.345	2.50	23.58	33.14	-14.02	.3243	.1847
4	48.940	-21.787	13.580	35.364	2.75	21.32	34.90	- 7.74	.2840	.1514
5	56.100	-21.787	17.160	38.942	3.00	19.47	36.63	- 2.31	.2500	.1250
6	68.200	-21.787	23.200	44.988	3.50	16.60	39.80	6.60	.1967	$.8725 \times 10^{-1}$
7	31.880	-31.880	0	31.880	2.53	23.28	31.88	-31.88	.3191	.1803
8	40.900	-31.880	4.600	36.390	2.82	20.77	25.37	-16.17	.2739	.1434
9	48.940	-31.880	8.5300	40.410	3.11	18.76	27.29	-10.23	.2367	.1152
10	56.100	-31.880	12.110	43.990	3.41	17.05	29.16	- 4.94	.2051	$.9288 \times 10^{-1}$
11	40.900	-40.900	0	40.900	3.15	18.51	18.51	-18.51	.2322	.1119
12	77.920	-21.787	28.067	49.854	4.00	14.48	42.55	13.59	.1579	$.6275 \times 10^{-1}$
13	87.540	-21.787	32.870	54.670	4.62	12.50	45.37	20.37	.1232	$.4326 \times 10^{-1}$
14	100.408	-21.787	39.300	61.108	5.75	10.02	49.32	29.28	$.8319 \times 10^{-1}$	$.2399 \times 10^{-1}$
15	48.387	-21.787	48.290	0.097	8.50	6.750	55.04	41.54	$.3987 \times 10^{-1}$	$.7960 \times 10^{-2}$
16	158.210	-21.787	68.210	$\to 90$	$\to \infty$	$\to 0$	68.21	68.21	$\to 0$	$\to 0$

$\theta_*^+ = \theta - \nu(M)$

$\theta_*^- = \theta + \nu(M)$

$$\theta - \theta_*^{\stackrel{-}{+}} = \stackrel{-}{+} \nu(M)$$

where the superscripts (-) and (+) refer to waves whose Mach waves

have slopes $dy/dy = \tan(\theta \pm \alpha)$, respectively.

The underlined numbers refer to the quantities known at the

beginning of the computation of the other quantities in each row.

Throughout all the computations, Helium is assumed to be a perfect

plasma gas.

The Mach wave pattern constructed are illustrated in Fig. 2.6.

Figure 2.7 shows the plot of the density and temperature variations

of the escaping jet in the x-direction for two vertical distances

(y = 0 cm and 0.25 cm) away from the axis of symmetry. In Fig. 2.8,

the variation of the same parameters in the vertical direction are

plotted for the planes x = 1 cm and x = 2 cm away from the orifice.

In Figures 2.7 and 2.8, the dimensionless ratios ρ/ρ_t^* and T/T_t^* have

been utilized rather than the absolute density ρ and temperature T

in order to make the results more general. In this way, the results

are independent of the initial beam density and temperature.

The theoretical model predicts that at the vicinity of the

hole, the injected plasma flow maintains the same density and tempera-

ture of the incident plasma. It is found that the initial state

extends within a triangular region formed by the initial Mach lines

originated from the two corners of the opening. As the injected flow

---

*The subscript t refers to the total conditions that would exist if
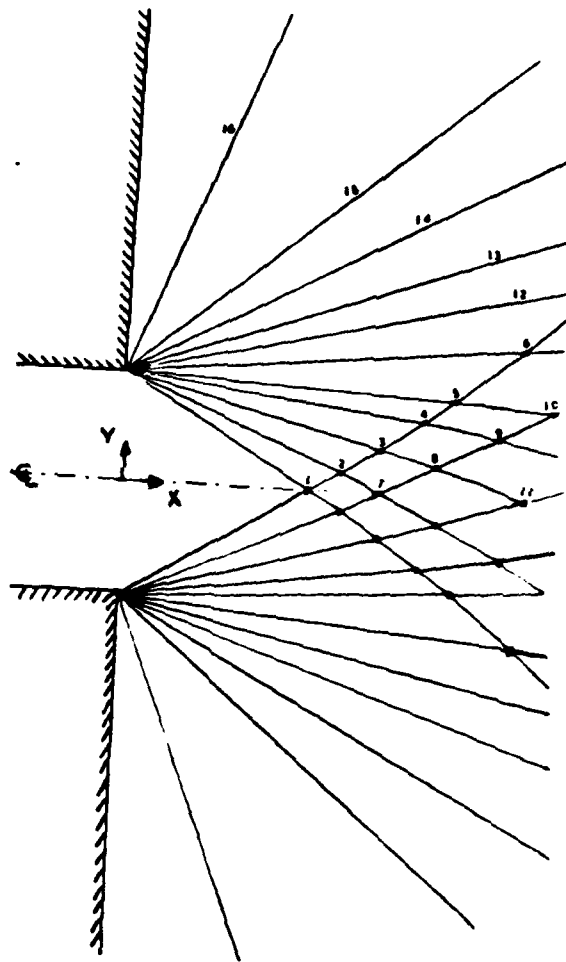the gas were brought to rest isentropically[21].

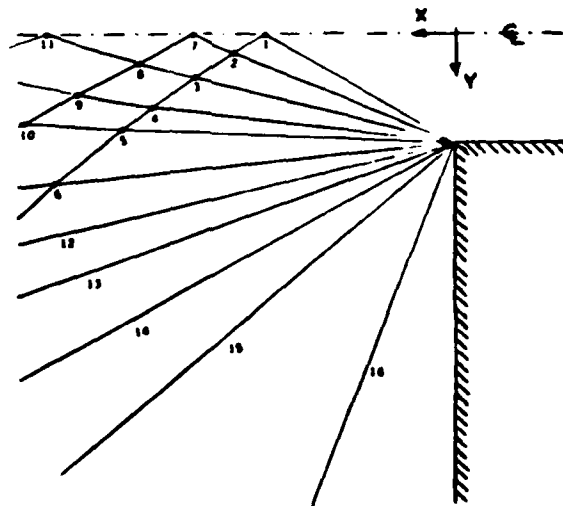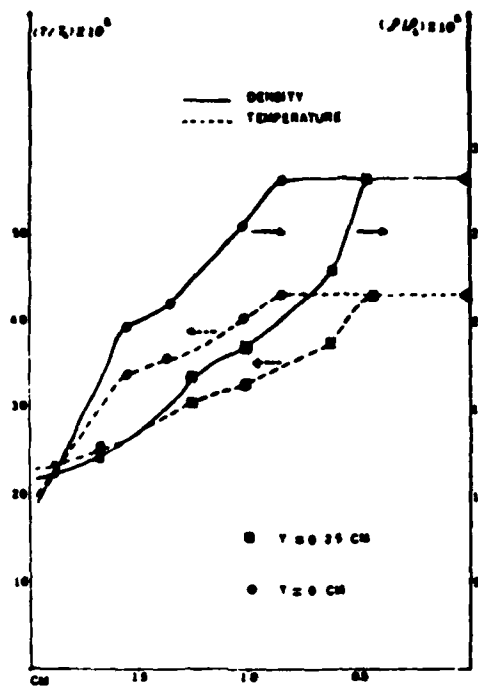Figure 2.6.   Mach Wave Pattern Through a Slit

for M = 2.

Figure 2.7. Density and temperature variations of the
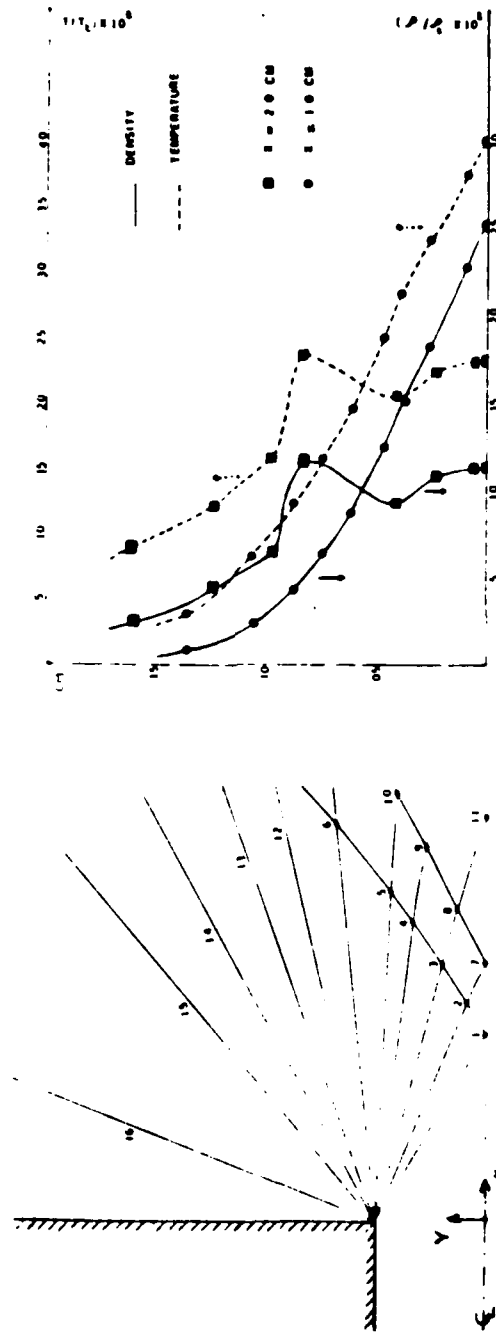
escaping jet in the axial direction for M = 2.

Figure 2.8. Density and temperature variations of the escaping jet in the transverse direction for M = 2.

expands further down the orifice, the density and temperature of the flow decrease significantly, but it is found that within 2 cm away from the hole, the total mass density of gas required for the Shiva experiment is fulfilled.

2.5 General Behavior with Mach Number M

Due to the value of the initial Mach number M, the Mach wave pattern for the jet has to be modified. A plot predicting the dependence of the initial Mach wave angle θ_1 and the escaping flow angle θ_2 on the Mach number M is represented in Figure 2.9. The change in the flow angles θ_1 characterizing the same parameters of the initial state of the plasma beam affects the spatial extent X_1 of the triangular region as shown in Fig. 2.10. It is concluded that high Mach numbers will produce smaller initial angles extending the initial plasma state further down the hole. Also, the change in the escaping flow angle θ_2 as the initial Mach number M is varied causes a change in the extent X_2 of the plasma mixing region when more than one hole is considered in the plate. Fig. 2.11 shows a plot of the dependence of the extent X_2 on the initial Mach number M. One notices that for low Mach numbers, due to the presence of multiple holes, the plasma mixing takes place at the vicinity of the holes while, at higher Mach numbers, no mixing region from the neighboring holes is expected.

Optimizations have to be made in order to get both large extent of plasma initial state and plasma mixing region in the Shiva
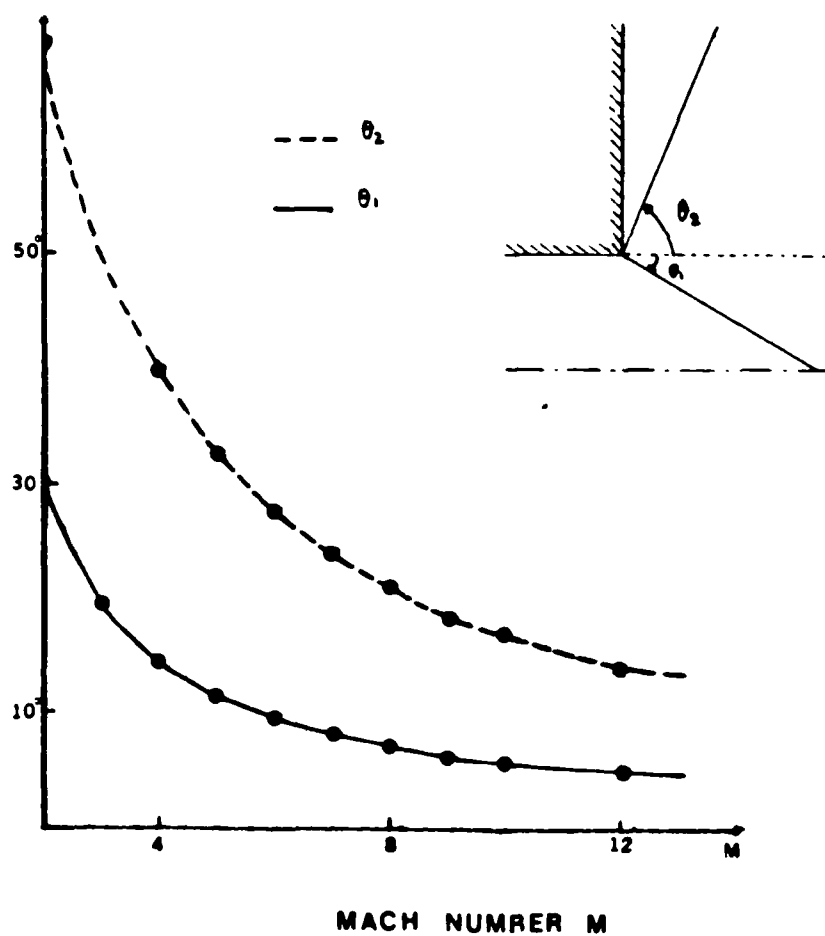
MACH NUMBER M

Figure 2.9. Dependence of the initial Mach Wave angle θ_1 and the escaping flow angle θ_2 on the Mach Number M.

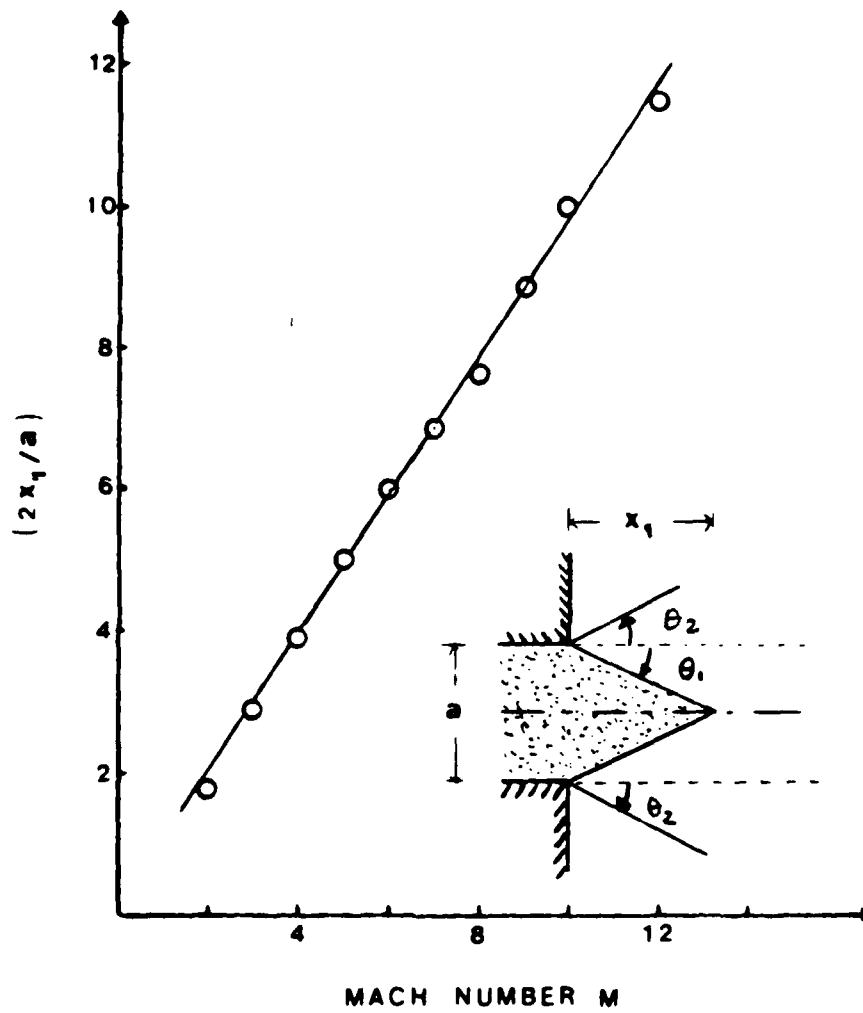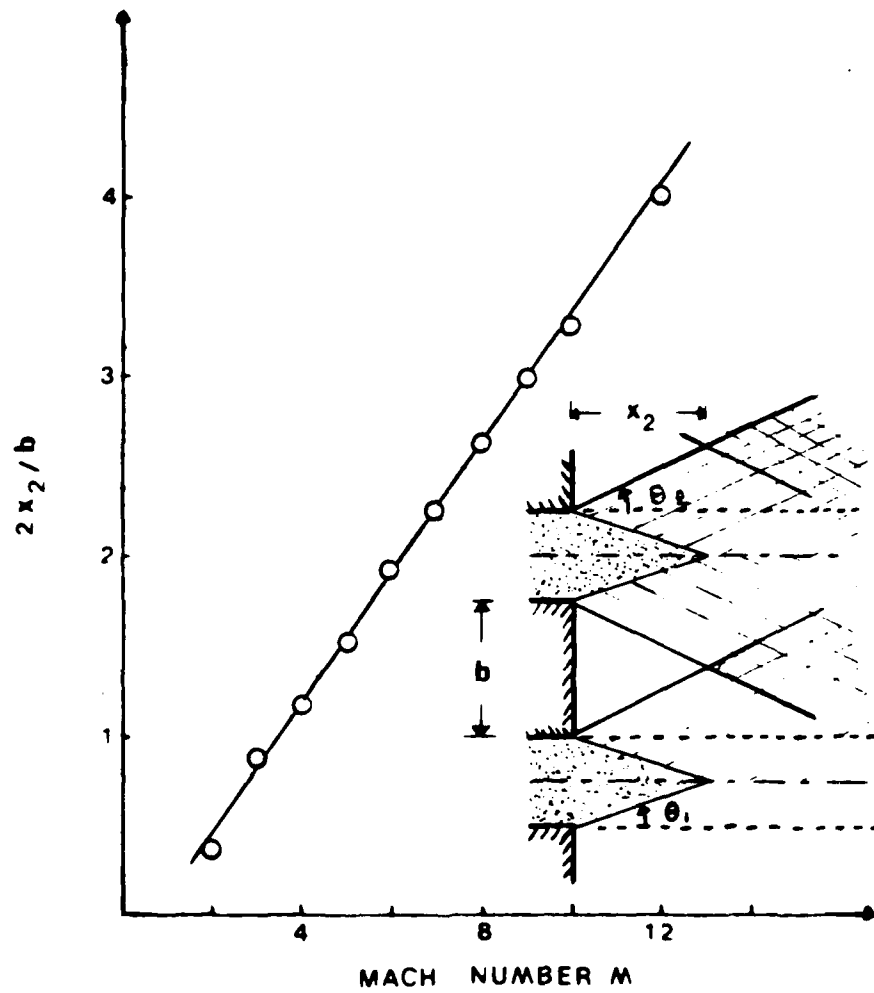Figure 2.10. Continuation of the plasma initial state on the Mach Number M.

Figure 2.11 Dependence of the plasma mixing region for

multiple holes on the Mach Number M.

implosion chamber.

A more appropriate solution to the proposed injection problem is
to use a circular hole in the plate instead of one dimensional slit
and use cylindrical coordinates for the solution of equations (2.4)
and (2.6), but the two characteristics on the hodograph plane and the
physical plane are not decoupled, as for the rectangular case[15] and
thus requires computer solutions to perform the many iterations
necessary to solve the problem. A computer program is not presently
available to carry out these calculations and should be the subject
of further study.

CHAPTER III

EXPERIMENTAL ARRANGEMENT AND DIAGNOSTIC TECHNIQUES

The experiment and the diagnostic techniques performed were
chosen to provide a means of testing the feasibility of the Shiva
plasma injection concept.

The plasma beam generated as part of this work was also inves-
tigated and characterized to determine its appropriateness to testing
the Shiva plasma injection concept.

3.1 Experimental Arrangement

3.1.1 General description

The beam is produced with an improved version of Cheng's plasma
gun,[9] a coaxial gun of conical shape with 0.7 cm inner electrode
radius and $\sim$ 4 cm mean outer electrode radius. The gun was contained
in a Pyrex glass tube where most of the experiments were carried out.
The whole system was evacuated to a pressure of $\sim 10^{-6}$ Torr.

The rest of the experimental apparatus was comprised of the main
energy storage capacitor bank, an electromagnetic valve for gas
puffing with related energy storate capacitor, the charging high vol-
tage system, the electronic triggering units and various diagnostic
equipment. An illustration of the experimental arrangement is shown
in Figure 3.1. The schematics of the energy storage bank and control
system for the plasma gun as well as the schematic of the trigger
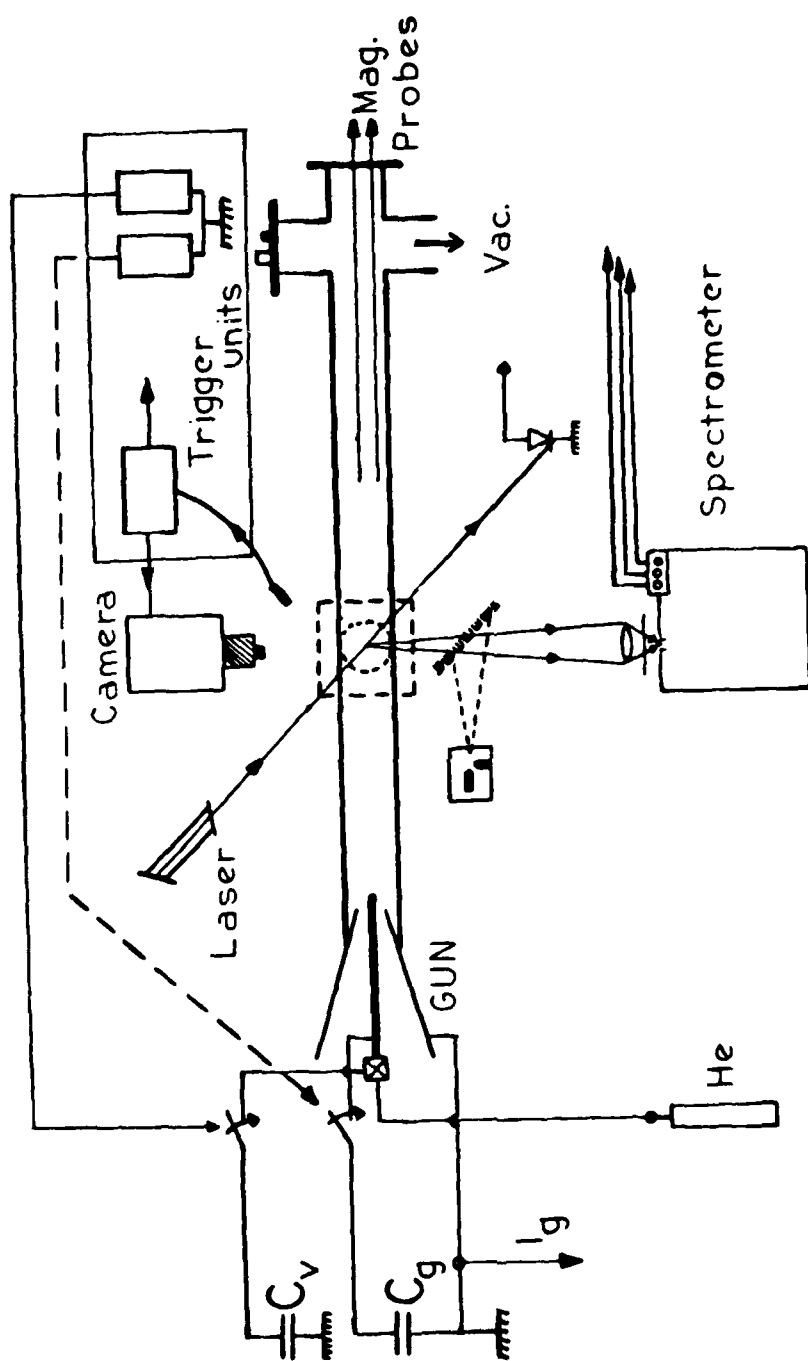unit can be found in Ref. 10.

24

Figure 3.1 Schematic of the experimental set-up.

3.1.2 Modifications

The gun is operated in the puff mode. In order to achieve the minimum densities for the Shiva experiment, estimated to be $\sim 10^{17}$ cm^{-3} for the He gas (Table 1.1), the original electromagnetic puff valve[10,11] had to be redesigned. The new version allowed more gas to be puffed into the gun.

While the control system remained the same as the one used by Lee[10], the energy storage system was revised for a better match of the capacitors to the gun thus assuring more efficient energy transfer. In particular, the gun switch has been removed altogether to reduce the system inductance.

A conducting back plate has been added to the original version of Cheng's gun.[22,23] This configuration causes faster breakdown of the gun and allows lower voltage operation. It also improved the reproducibility of the beam formation considerably. A schematic of the coaxial gun presently used is given in Figure 3.2.

In addition, many improvements have been made on electrical protection of the gun and the valve. Particular attention was given to grounding and shielding problems. The negative polarity of the inner electrode has been determined experimentally to be fundamental to the beam formation.

3.1.3 Mode of operation

The procedure of firing the gun is as follows: a 15μF energy storage capacitor is used to control the fast electromagnetic valve.

VACUUM FLANGE-Brass

RETAINING PLATE-Brass

ANODE-Stainless Steel

CATHODE-Steel

CATHODE PLUG-Tungsten

ANODE INSERT-Stainless Steel

INSULATOR-Quartz

VALVE HOUSING-Brass
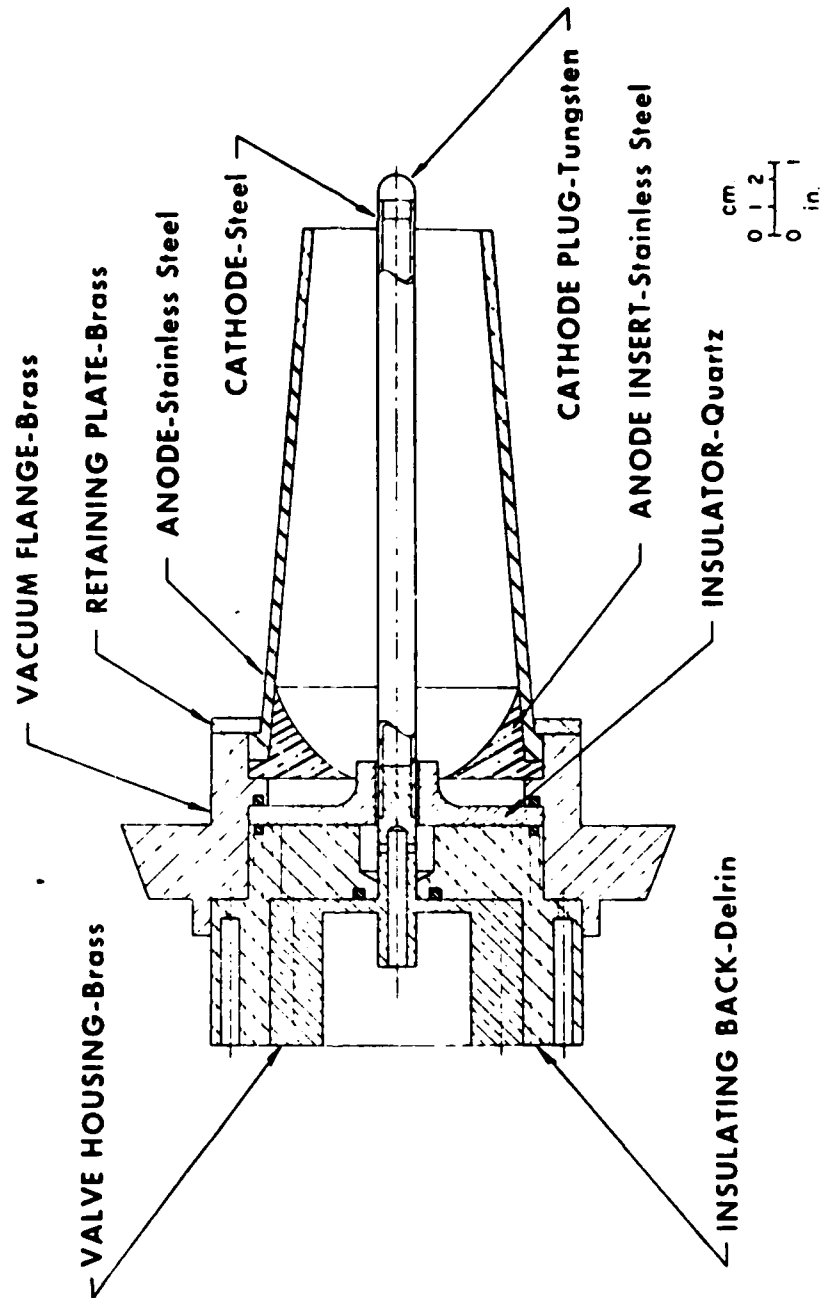
INSULATING BACK-Delrin

cm
0 1 2
0 in
1

Figure 3.2.   Schematic of the Coaxial Plasma Accelerator.

The back pressure of the valve and the on-time of the electromagnetic valve determine the amount of He gas puffed into the barrel of the gun. A 60µF low inductance capacitor bank charged to the proper voltage was permanently connected across the two electrodes of the gun.

An initial manually triggered pulse starts the valve capacitor to discharge causing a momentary opening of the valve allowing He gas to enter the barrel of the gun. The breakdown of the gun occurred when the Paschen conditions are reached. The time elapsed between the firing of the puff valve and the triggering of the gun is found to depend on the capacitor voltages and the background pressure of the valve.

The mechanism of the beam formation has been explained as a $\vec{J} \times \vec{B}$ force acting upon the electrons, while the ions experienced the Coulomb force acceleration due to the ejected electrons.[22] The current sheet is therefore accelerated down to the muzzle of the gun and then collapses in front of the inner electrode resulting in the ejection of a high density high velocity plasma beam.

3.1.4 Simulation of the injection experiment

Initially, an interaction chamber made of brass material was inserted in the experimental set-up in order to study the beam-plate interaction. The presence of the interaction chamber, its shape and grounding have considerably changed the properties of the beam, producing appreciable return currents and modifying the beam characteristics.

In the next stage, the interaction chamber was removed and re-placed with Pyrex glass tubing.

For the interaction plates, initially Al or Cu plates were used. It was found out that the energetic plasma beam ablates a considerable amount of material from those electrodes. The light generated from these ablatants and the line impurities made the study of the beam hole interaction almost impossible. Therefore, these plates were re-placed by two tungsten plates separated by 0.5 cm, simulating a one dimensional slit representing the actual assumed theoretical model.

3.2 Diagnostic Techniques

The diagnostic procedures were directed towards the analysis of the beam features before and after the opening.

The diagnostic techniques performed to infer the different plasma parameters were mainly optical interferometry optical spectro-scopy, high speed visual photography and monitoring of the electrical parameters of the gun system. These will be described separately below.

3.2.1 Optical interferometry

Within the range of the electron densities produced by the gun an Ashby-Jephcott type laser interferometer[24] was found to be suitable for density measurements. The visible radiation of a He-Ne laser at 6328Å was used in the interferometer.

3.2.2 High speed photography

High speed visual photography measurements were made using an

STL image converter camera both in the framing and the streak mode.
The camera is triggered either optically or electrically.

3.2.3 Optical spectroscopy

The spectroscopic techniques used were concerned with the estimation of the He_I (5876Å) and He_{II} (4686Å) line intensities as well as the continuum intensity.

These measurements were performed by a McPherson (Model 2165) spectrometer. The integrated line spectra is recorded on a polaroid film. Slits to monitor the time history of the spectra corresponding to He_I, He_{II} and continuum were machined on phosphor   bronze metal strip and placed at the plane of the exit slit. Three photomultipliers were placed behind each slit and care is taken to match the outputs of the photomultiplier tubes to the characteristic impedances of the coaxial lines. The signals were monitored by a Tektronix 551 dual beam oscilloscope. A reference He gas discharge source is used for locating the various lines. The apparatus was calibrated by means of a carbon arc standard[25].

Since the time delay between the initial triggering of the valve and the breakdown of the gun was not reproducible, other means of initiating the diagnostic equipment such as the optical fiber or the gun current, were used. The time t = 0 was usually obtained by getting an optical trigger from the initial light output of the gun, while the initial rise in gun current was used to trigger the oscilloscope for some of the measurements.

The terminal currents and voltages of the gun were monitored by a Rogowski coil and capacitive voltage divider, respectively.

CHAPTER IV

EXPERIMENTAL RESULTS

4.1   Plasma Parameters

Experimental measurements were performed to provide a check on the theoretical calculations of Chapter 2.

One of the important parameters to be experimentally determined was the Mach number M. As pointed out in Chapter 2, M is defined as

$$M = \frac{V}{C} = \frac{V}{\sqrt{(\gamma kT/m)}} \tag{4.1}$$

In the plasma, the flow velocity V is defined as:

$$V = \frac{\rho_i v_i + \rho_e v_e}{\rho_i + \rho_e} \tag{4.2}$$

where ρ and v denote the density and velocity respectively, and the subscripts i and e refer to ions and electrons. Since the electron mass is much smaller than the ion mass, $\rho_e \ll \rho_i$, then the beam velocity can be taken equal to the ion velocity

$$V \approx v_i \tag{4.3}$$

Thus the momentum of the beam is carried by the ions. Using a similar argument, the temperature T used in expression (4.1) is described as follows. In a fully ionized ideal gas, the pressure P of the gas is the sum of the partial pressures P_i due to the ions and of P_e

32

contributed by the electrons.

$$P \equiv P_i + P_e \equiv nk(T_i + T_e) \tag{4.4}$$

Previous measurements on the ion temperature[23] have shown that the ions in the beam are cold, i.e., $T_i \ll T_e$, thus, the temperature T in the speed of sound (eq. 4.1) is taken to be equal to the electron temperature.

To evaluate the initial Mach number of the beam, the parameters therefore required to be determined a priori, are the ion velocity and the electron temperature. The electron density is also of primary interest as well, although it is not needed for flow analysis, but it is necessary to verify the various assumptions made in the theoretical consideration as well as in spectroscopic analysis.

All these parameters are also required after the passage of the plasma through the central hole in the plate. The extent of the divergence of the plasma jet as it leaves the plate is also needed.

4.2 Beam Structure Measurements

Initial investigations of the beam parameters are focused on the evaluation of the beam parameters without the perforated plate.

4.2.1 High speed photography

A typical set of image converter camera framing pictures of the beam taken for different time intervals at 50 nS exposure time are shown in Figure 4.1. These pictures reveal that the beam lasts for 5 ∿ 6 μs and stays uniformly collimated over ∿ 50 cm. The

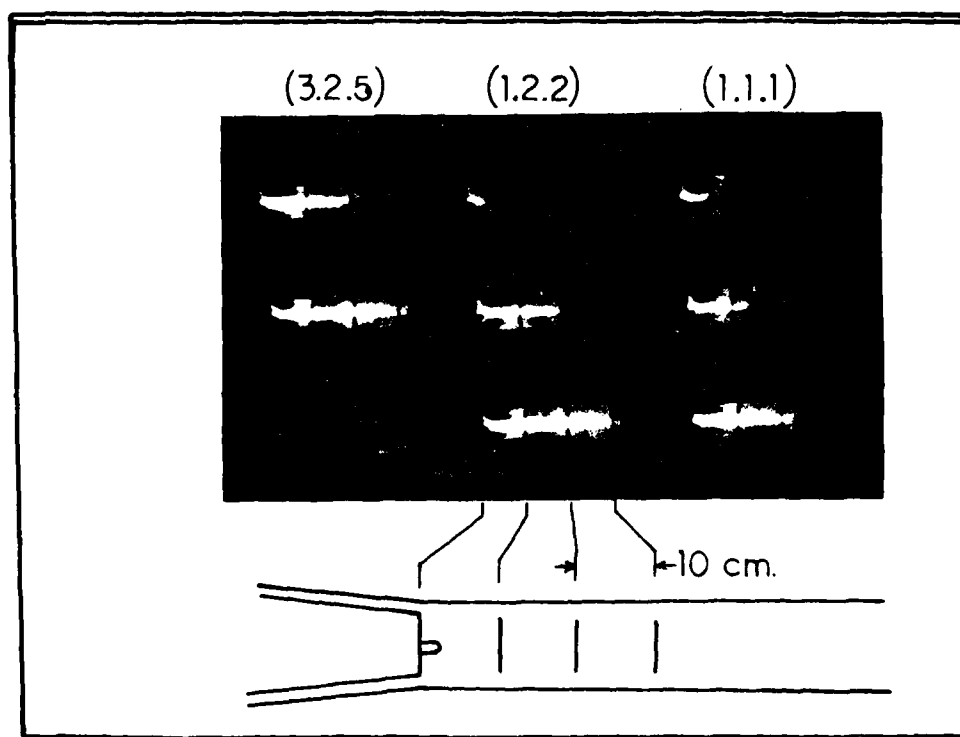Figure 4.1. Typical set of image converter camera

framing pictures (50 nsec exposure)

V_G = 9 kV; V_v = 8 kV;   p = 2 psi

diameter of the beam is found to be 2 $\sim$ 3 cm.

The beam velocities are determined from the streak pictures using an STL camera. A slit 1 mm wide was placed along the axial length of the Pyrex pipe with strips equally spaced every 5 cm for spatial identification. A total time exposure of 10 μs was used for the streak pictures. A typical set of streak pictures taken for different gun voltages at a given back pressure (2 psi) is shown in Figure 4.2. The valve voltage was kept constant at 8 kv. It was found that the initial beam front propagates with a velocity of 10 $\sim$ 20 cm/μs depending on the gun voltage and the back pressure of the valve and travels $\sim$ 50 cm down the Pyrex tube verifying the framing picture observations. The dependence of the initial velocity of the beam on the gun voltage and the valve back pressure is plotted in Figure 4.3. It was found that at later stages of the beam, the beam velocity decreases. The velocity-time history of the beam for different gun voltages and different valve back pressures is illustrated in Fig. 4.4. Figure 4.5 represents the velocity-time history of the beam for different gun voltages but for a given valve back pressure ($\sim$ 1 psi). In figures 4.4 and 4.5, the velocities are normalized to the initial velocity V_o. The time dependence of the beam indicates that the velocity decreases constantly towards the trailing edge. The streak picture also verify that the lifetime of the beam is $\sim$ 5 μs consistent with the framing pictures.

At low gun voltages the beam parameters were not easily reproducible indicating an erratic form for the beam.

$V_G = 6$ kV

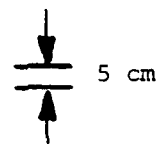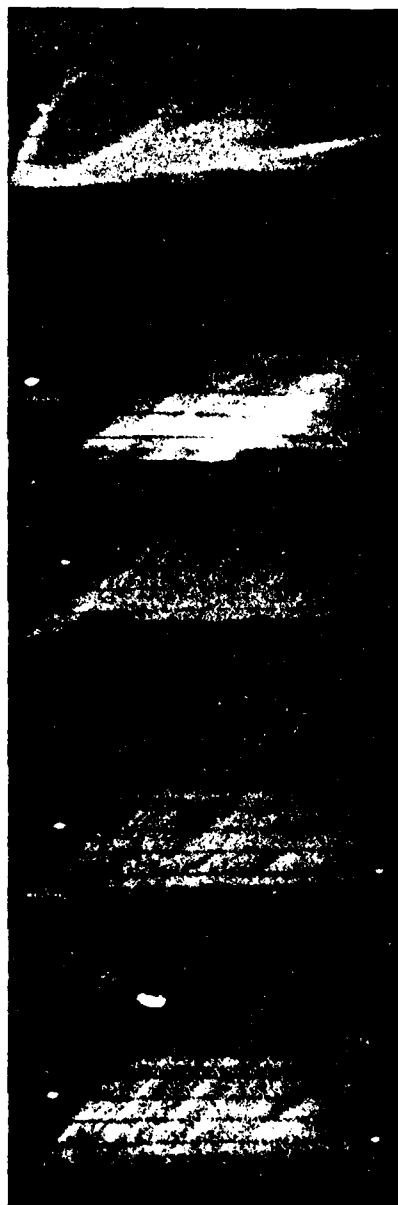$V_G = 7$ kV

$V_G = 8$ kV

$V_G = 9$ kV

5 cm

$V_G = 10$ kV

Figure 4.2 Typical set of streak pictures of the beam for

different gun voltages (V_G).

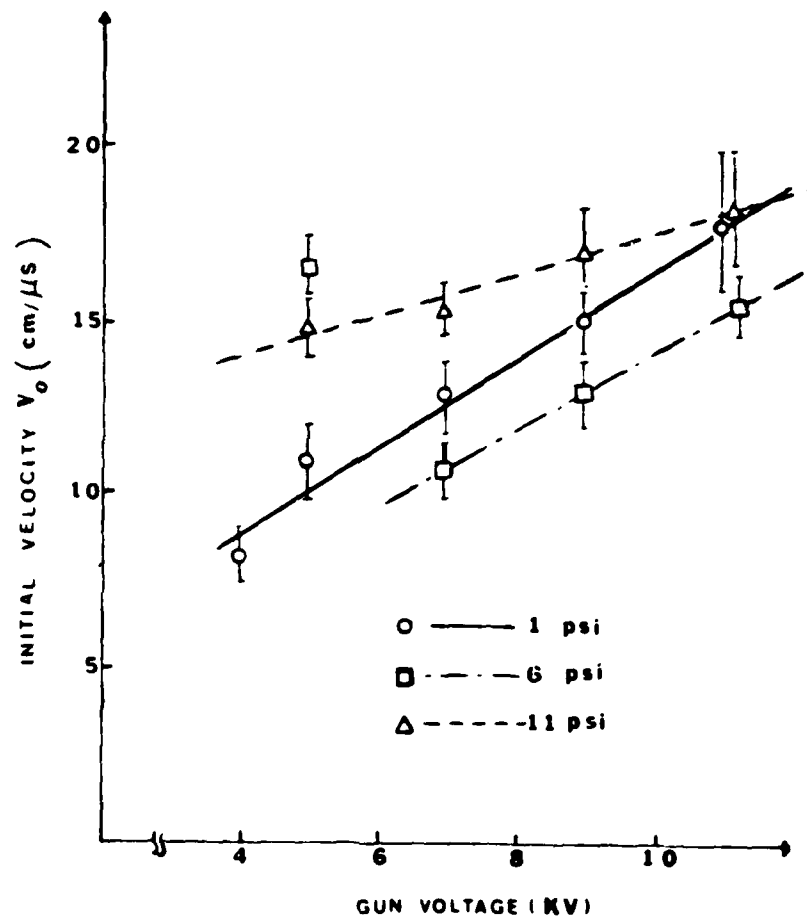Total streak time = 10 μsec. $V_V = 8$ kV,   p = 2 psi.

Figure 4.3. Dependence of the initial velocity of the beam on gun voltage and back pressure.
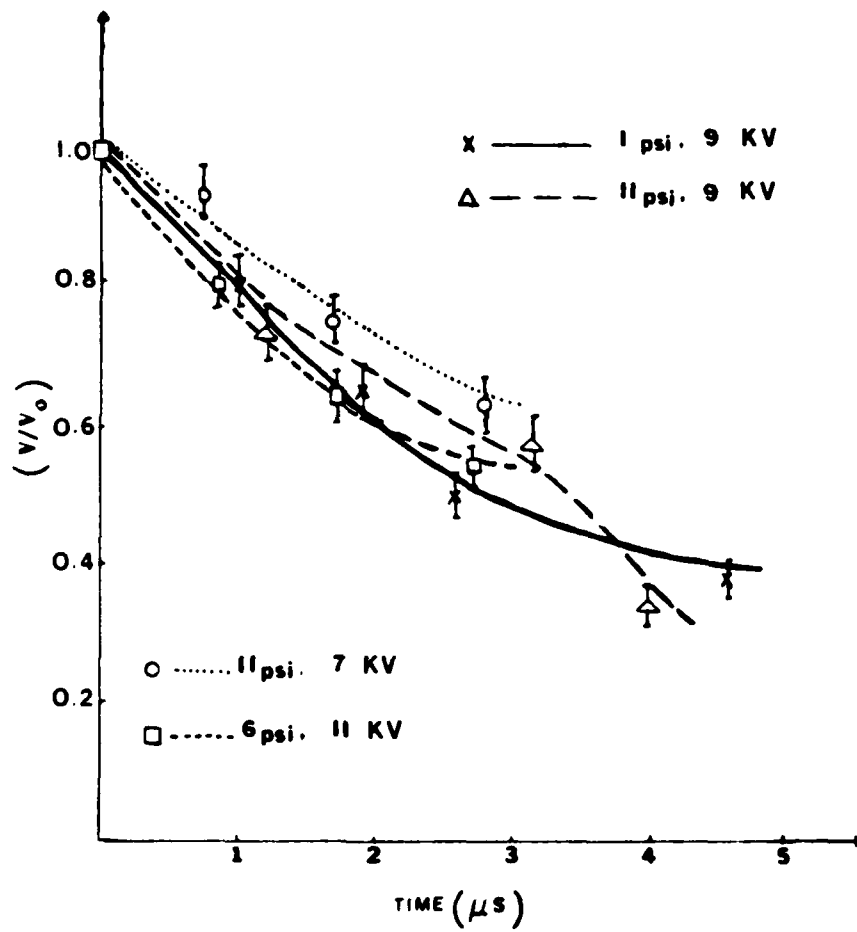
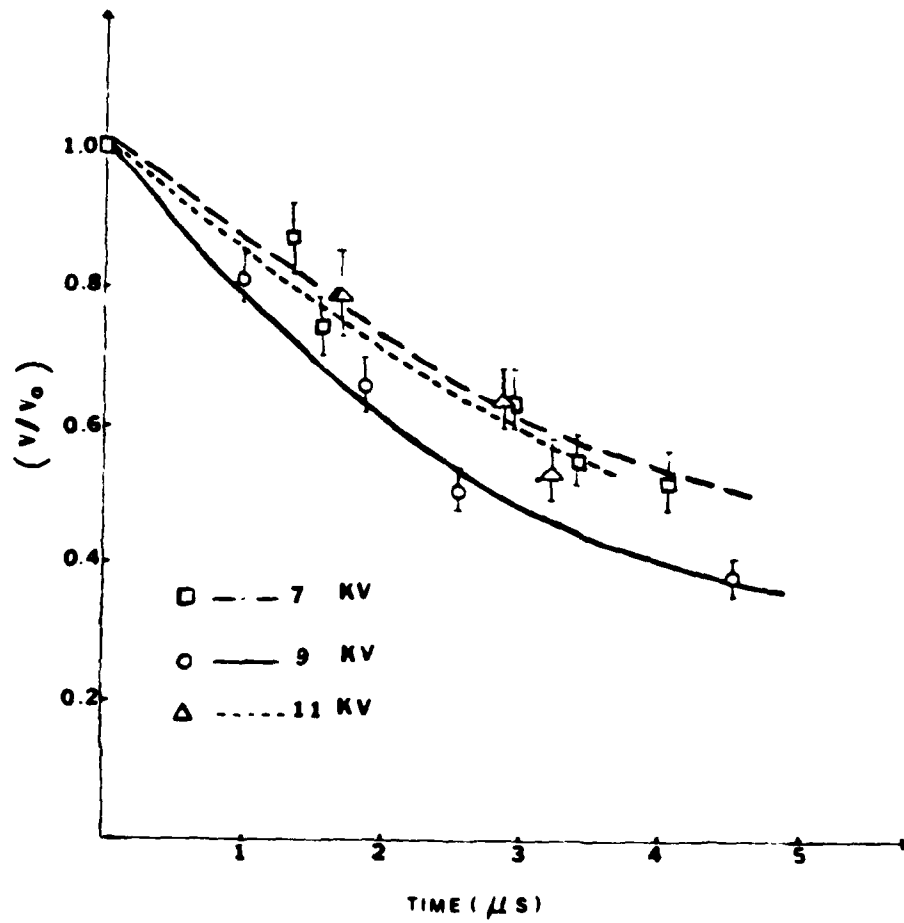Figure 4.4. Velocity time variation of the beam.

Figure 4.5. Velocity time variation of the beam at a given back pressure 1 psi.

For later analysis on the understanding the dynamics of the beam formation terminal current and voltage characteristics of the gun were also recorded. Typical current and voltage waveform for the gun are shown in Figure 4.6.

4.2.2 Spectroscopic techniques

a) General Remarks

The literature deals extensively with both the theory and experiments, on the radiated intensities of the He_I, He_{II} lines as well as the continuum intensity. Theoretical curves relating various ratios of these intensities as a function of temperature are given in Ref. 26.

The spectroscopic techniques used to determine the plasma parameters are based upon the assumption of local thermodynamic equilibrium (LTE)[26,27,28,29] for the plasma. For this assumption to be valid, the required electron density should be higher than the minimum electron density Ne given by Griem[26]

$$N_e \approx 2.2 \times 10^{16} \ cm^{-3} \quad at \quad T_e = 4 \ eV$$

$$N_e \approx 6.6 \times 10^{16} \ cm^{-3} \quad at \quad T_e = 36 eV$$

To locate a region for continuum intensity measurements free of impurities, integrated line spectra of the beam radiation is recorded through a McPherson spectrometer using a polaroid film. The integrated line spectra of $He_I(5876\overset{o}{A})$ and $He_{II}(4686\overset{o}{A})$ were also

5 V/cm

0.1 V/cm

(a)

(b)

$\dashv$ $\vdash$ 5 µsec/cm

Figure 4.6 Typical current and voltage waveforms for the gun.

a) gun current   b) gun voltage

V_G = 9.5 kV V_v = 9.5 kV   p = 6 psi
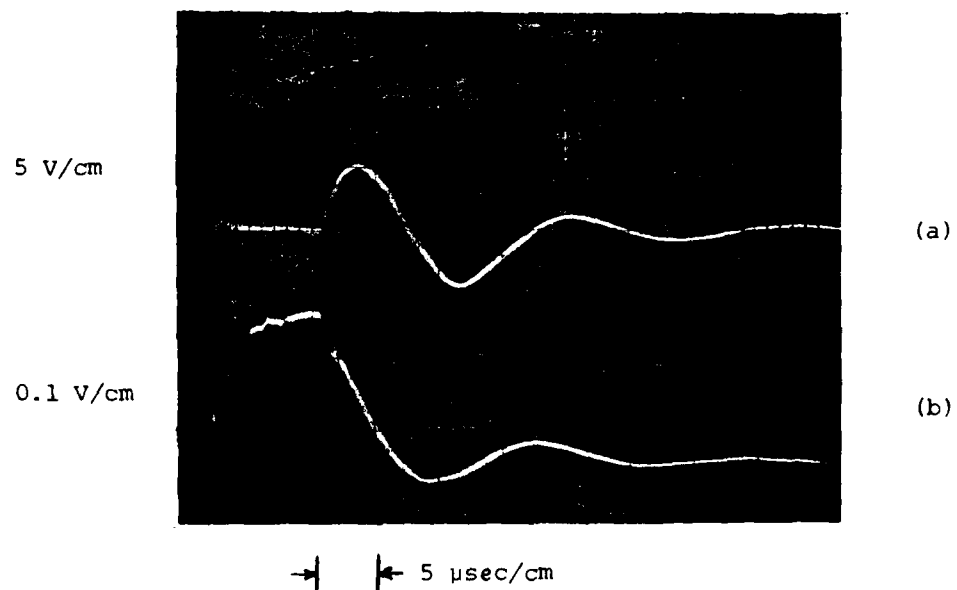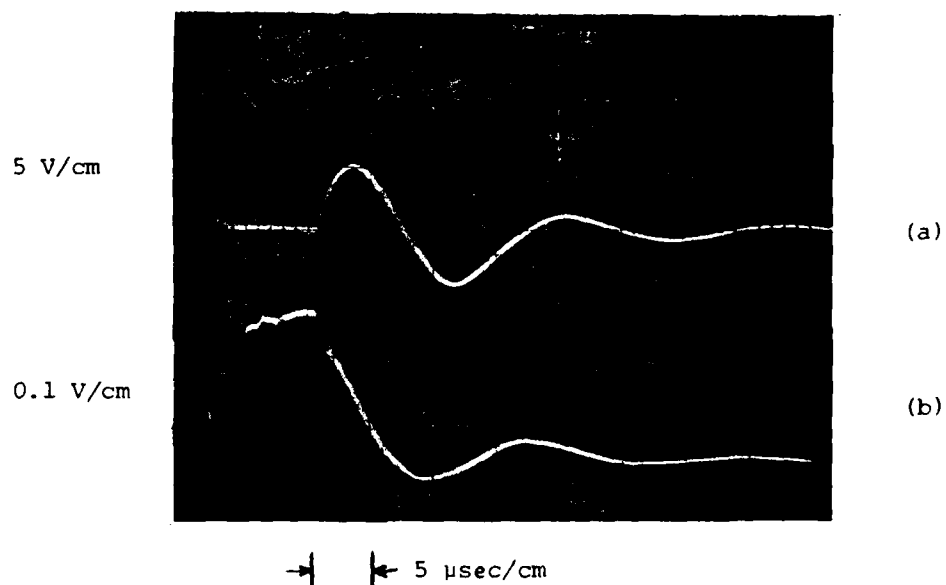
5 V/cm

0.1 V/cm

(a)

(b)

→| |← 5 μsec/cm

Figure 4.6 Typical current and voltage waveforms for the gun.

a) gun current   b) gun voltage

V_G = 9.5 kV V_V = 9.5 kV   p = 6 psi

recorded on the same film. The radiation spectrum of the beam taken at 10 cm from the muzzle of the gun is shown in Figure 4.7b. The pictures revealed that no He_I (5876Å) line was recorded even when 25 shots were superimposed on the same film. This suggested that the plasma beam had a higher electron temperature than previously reported[23]. For the continuum a region free of impurity lines was selected, centered at 5559Å.

b) Temperature Measurement

Typical photomultiplier signals giving the intensities of the continuum radiation and He_{II} (4686Å) line are shown in Figure 4.8a. The He_I line intensity was found to be of the same magnitude as the corresponding continuum intensity at the He_I location which was determined from a calibrated mask using a standard He gas discharge tube. The slits in the mask were made at the He_I, He_{II} and continuum with openings of 14.1Å, 5.6Å, and 12.7Å, respectively.

The ratio of the total intensity of the He_{II} line to the intensity of the underlying continuum (100Å wide) centered at 4686Å has been employed to evaluate the beam temperature. From the curve taken from Ref. 26 and shown in Figure 4.9 gives $T_e \sim (42 \pm 5$ eV). An interpolating formula has been used to calculate the continuum centered at He_{II} line from the 5559Å continuum.[26]

The time variation of the beam electron temperature for gun voltages of 9 kV and 10 kV is shown in Figure 4.10. Higher electron temperatures have been recorded for lower voltages. It was also
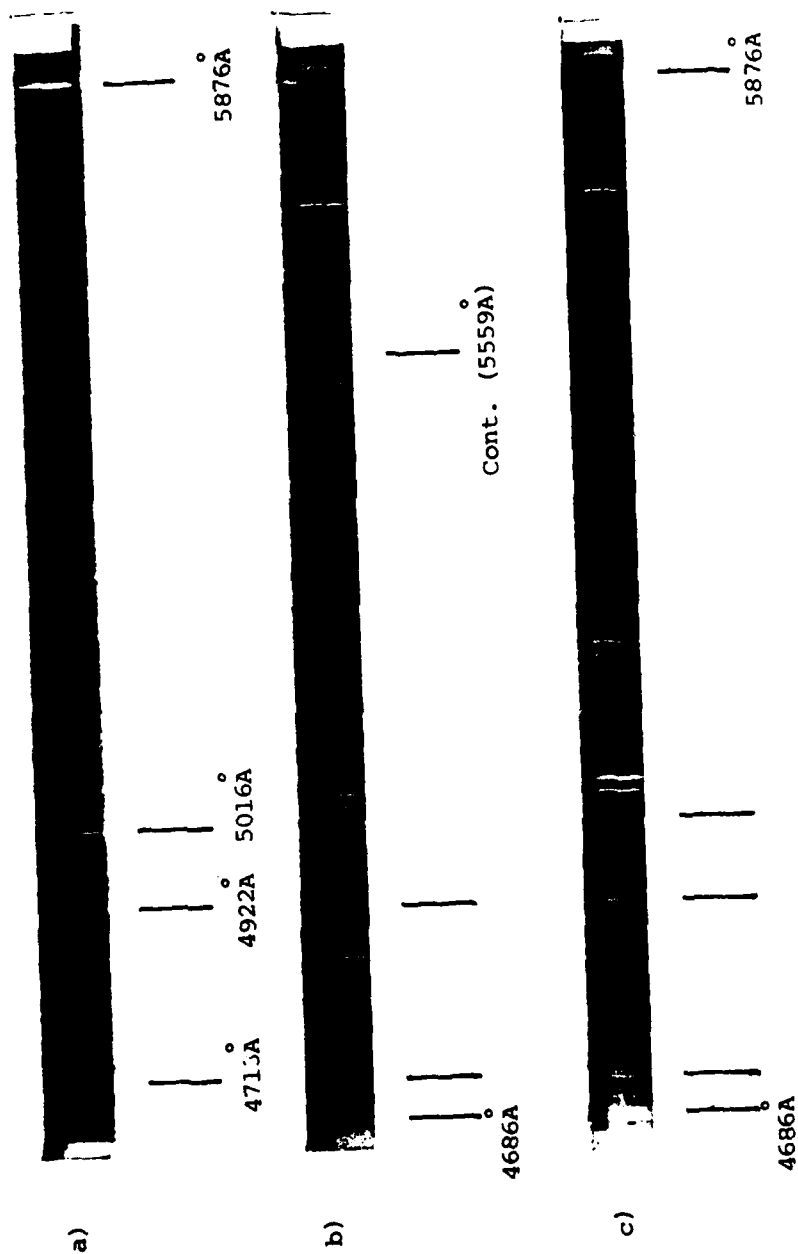
Figure 4.7. Integrated line intensities of the plasma beam
a) He tube discharge (Reference); b) the beam at 10 cm away from
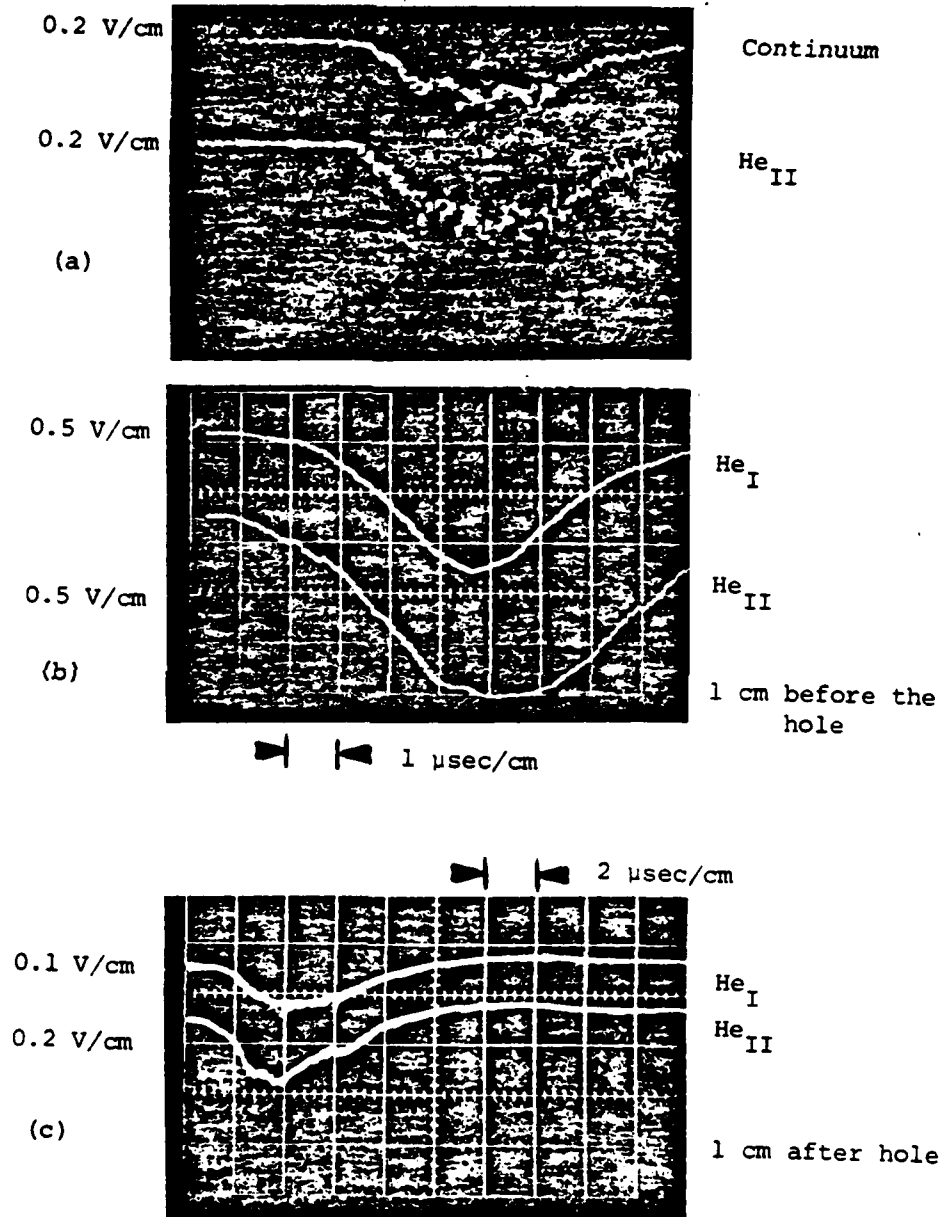the muzzle of the gun; c) the beam in the presence of the plate.

0.2 V/cm

Continuum

0.2 V/cm

He$_{II}$

(a)

0.5 V/cm

He$_I$

0.5 V/cm

He$_{II}$

(b)

1 cm before the hole

1 μsec/cm

2 μsec/cm

0.1 V/cm

He$_I$

0.2 V/cm

He$_{II}$

(c)

1 cm after hole

Figure 4.8 Typical photomultiplier signals.

$V_G = 9$ kV $V_{v.} = 8$ kV   p = 2 psi
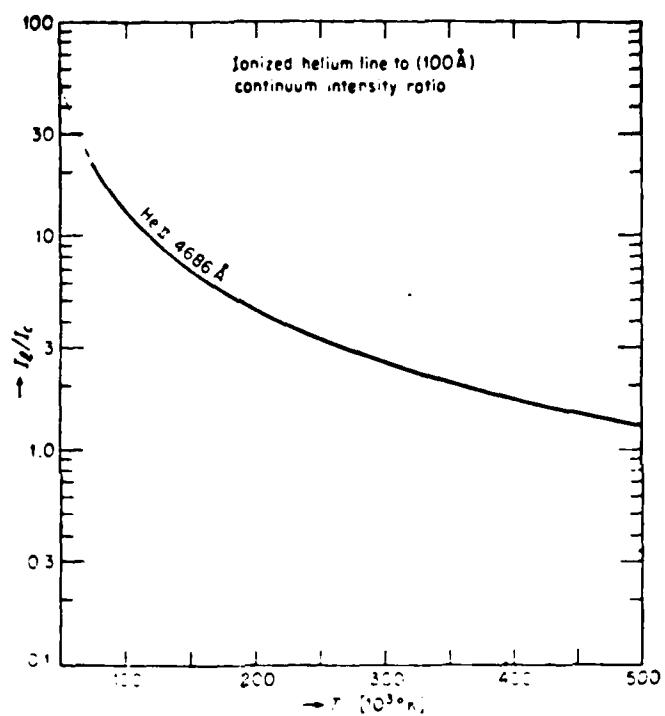
Ratio of the total line and continuum intensities (in 100-Å bands centered at the lines) as a function of temperature for ionized-helium lines. (Ref. 26)
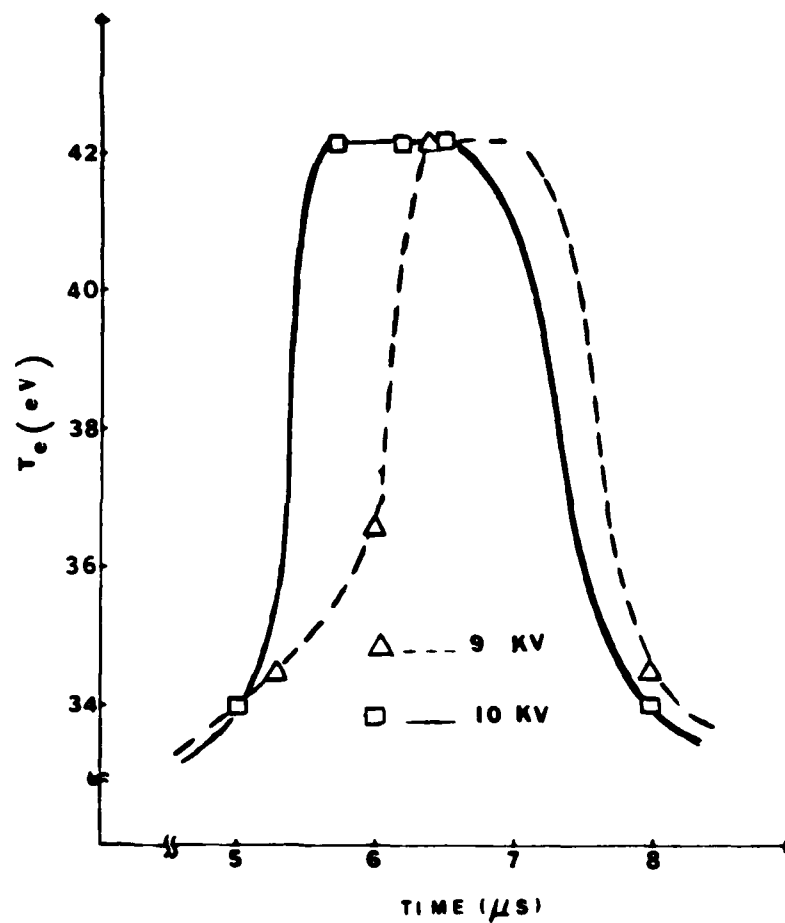
Figure 4.9

Figure 4.10. Temperature History of the Beam.

observed that the maximum temperature is maintained for about a few microseconds.

c) Density measurement

The electron density was obtained from the absolute continuum intensity measurements.[30,31] A carbon arc standard was used for calibrating the photomultipliers.

The working expression relating the voltage ratio between the pressure of the carbon arc and the continuum intensity is given by

$$N_e = 1.07 \times 10^{17} \sqrt{V_C/V_S} \ cm^{-3} \tag{4.5}$$

where V_C and V_S are respectively the photomultipliers output voltages for the continuum intensity (5559Å) and carbon arc standard.

The electron density N_e has been found to increase linearly with the gun voltage and reaching $(2\pm0.25)\times10^{17} \ cm^{-3}$ for a gun voltage of 11kV as shown in Figure 4.11. The density time-history of the beam for different gun voltages is also plotted in Figure 4.12. The value of the electron density thus measured, fulfills the requirements of both the Shiva experiment (Chapter 1) and the LTE assumptions.

4.2.3 Optical interferometry

The laser interferometry technique is initially used in the presence of the interaction chamber to determine the electron density of the beam. The relationship between the number of fringes N detected and the electron density N_e of the plasma beam for 6328Å laser
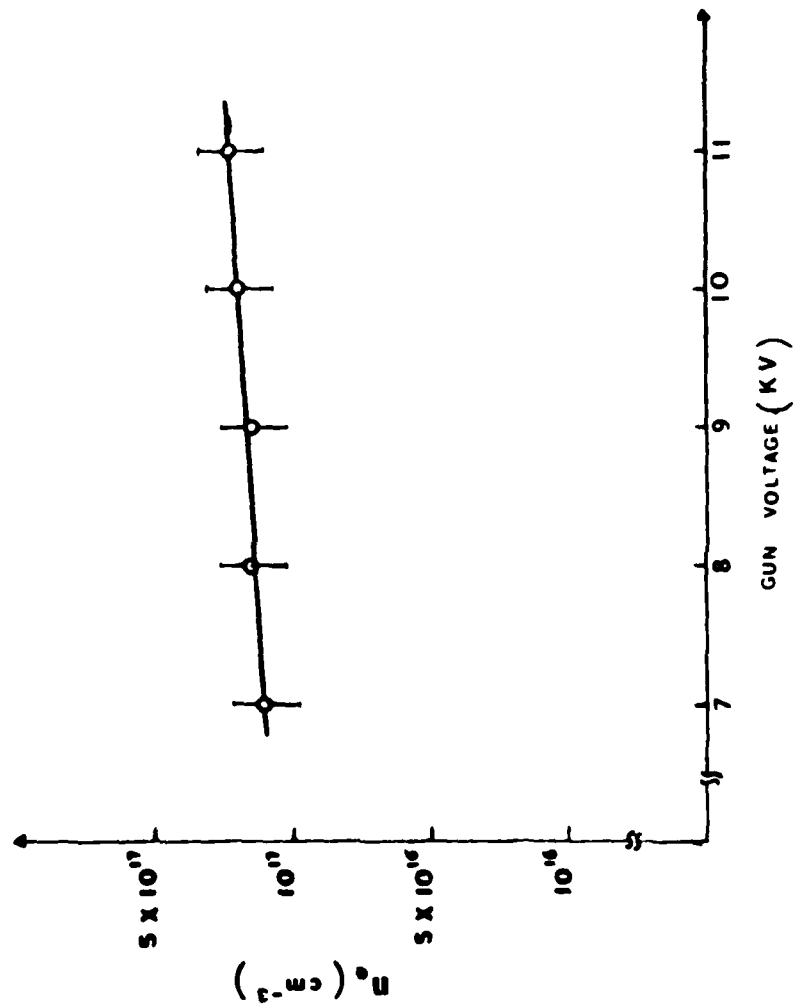
Figure 4.11 Dependence of the maximum beam electron density on the gun voltage.
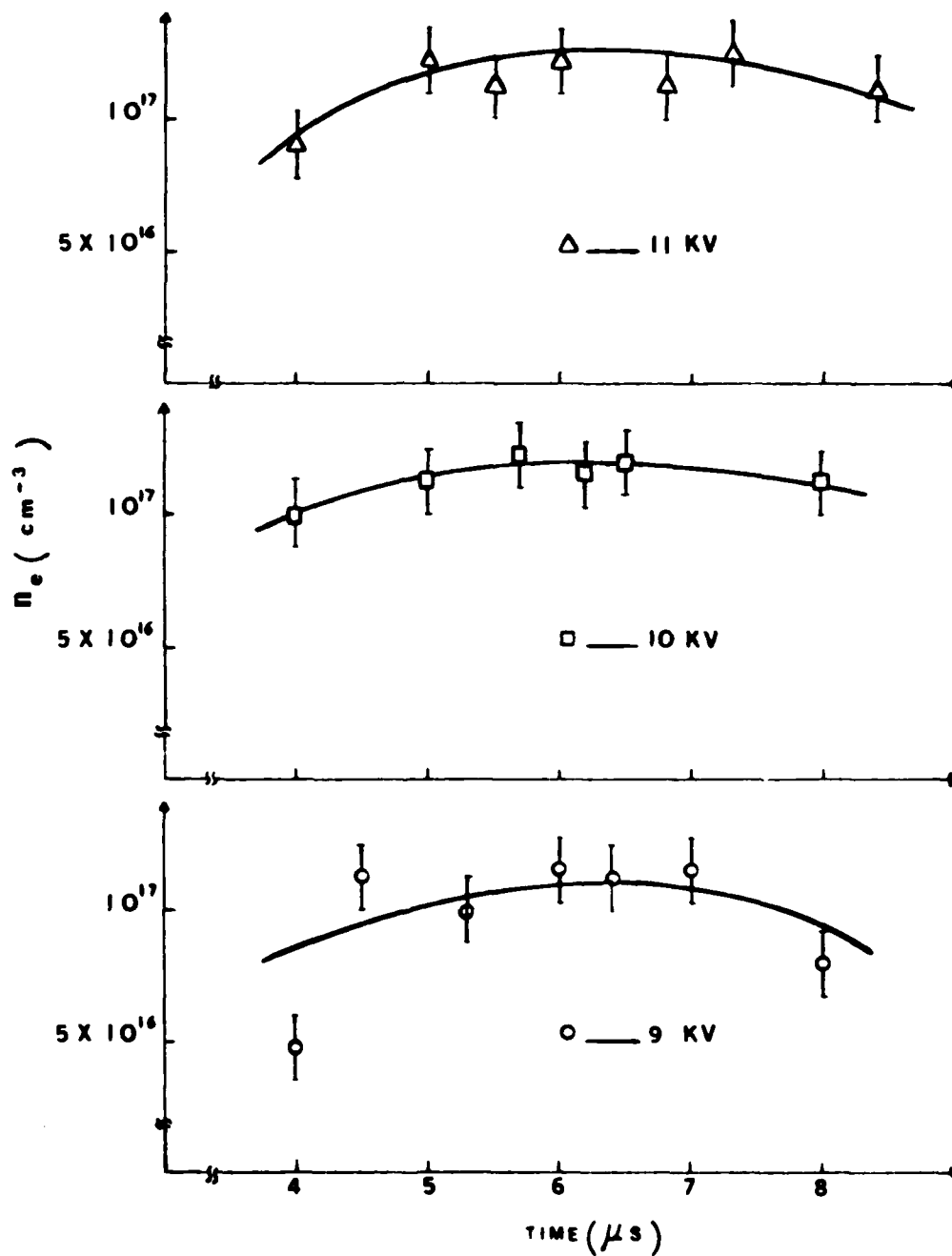
Figure 4.12. Variations of density for different gun voltages.

radiation[24] is given by

$$N = 5.6 \times 10^{-18} N_e \qquad (4.6)$$

Using the Ashby-Jephcott interferometer, the following interference fringes are obtained as shown in Figure 4.13. From these interference fringes, an average electron density of $N_e \simeq 4 \times 10^{17}$ cm^{-3} is obtained. This value is within the range of the electron density values obtained using the optical spectroscopic techniques.

4.3 Beam-Hole Interaction

An Al or a Cu plate, 6.25 mm thick, having a central circular hole one cm in diameter was placed 10 cm in front of the gun.

The usual observation of the appearance of the plates, Figures 4.14 a,b indicated that considerable electrode material was ablated from the hole region. The light produced by the Al and Cu metal vapor had lines very close to the 6328Å laser radiation, (Al$_{II}$:6336Å; Cu:6326Å; Cu$_I$:6325Å; Cu$_{II}$:6318Å), thus interfering with and making it impossible to use the laser interferometry technique with the existing equipment. It was also found that a metal impurity line appeared at the continuum slit making it impractical to use the existing continuum location for spectroscopic diagnostics.

Observations showed that the ablation from the interaction plate was of the same order of magnitude whether the plate is placed inside the interaction chamber or in a Pyrex tube alone. Therefore, due to the possibility of current loops, the interaction chamber was removed

a)

b)

1 µsec/cm
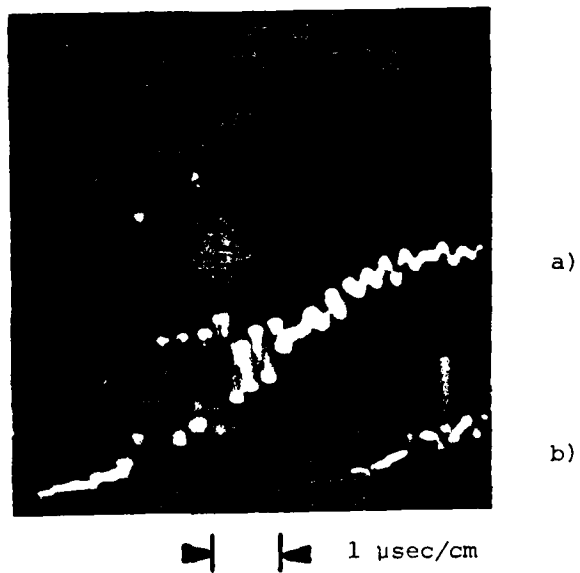
Figure 4.13.   Interferometer output for the plasma beam

a)   with the plasma

b)   without the plasma.

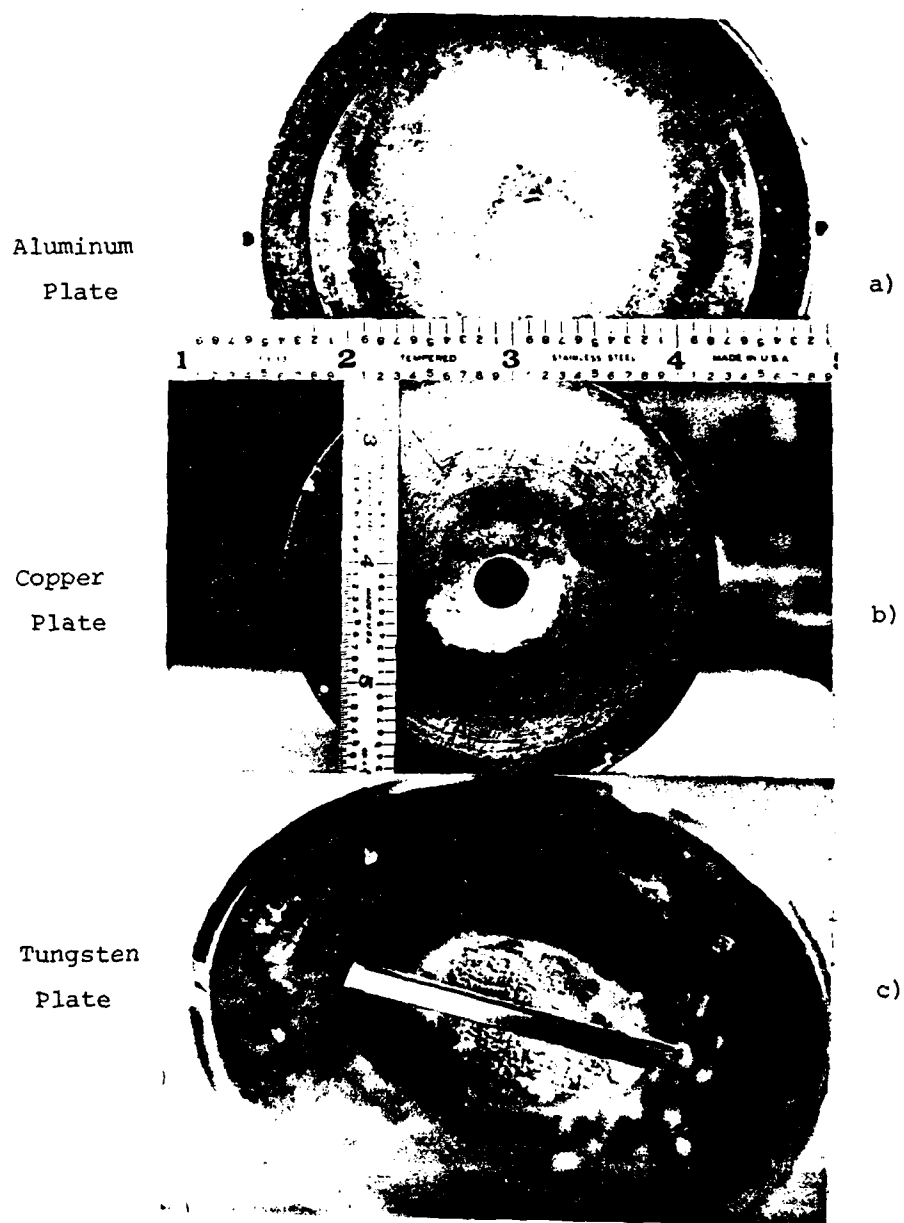Aluminum
Plate

a)

Copper
Plate

b)

Tungsten
Plate

c)

Figure 4.14. Ablation of the different plates. The high

ablation is clearly visible in the pictures.

and only a Pyrex pipe and an interaction plate were used.

Later, similar experiments were repeated for which the hole was replaced by a 5mm slit made from two tungsten plates 2mm thick as illustrated in Figure 4.14c.

As expected the presence of an obstacle in front of the beam reduced the beam velocity. The velocity of the escaping jet was found to be approximately 5-10 cm/μs. This was obtained from streak pictures of the beam after it emerged from the slit. Typical streak pictures shown in Figure 4.15 indicated that the jet traveled a length of 10cm and lasted for about 5 μs verifying the steady state assumption stated earlier. Figure 4.16 gives the velocity time-history of the beam beyond the hole.

An attempt was made to determine the incident velocity at the slit but due to the strong ablation of the material, and accompanying intense light, the STL camera was always overexposed making measurements very difficult.

For the Cu plate, the He_I line was observed in the time integrated spectra for the beam before the hole as shown in Figure 4.7c. It was found also that a Cu_I line (5555Å) fell within the slit opening of the continuum, making temperature and density measurements from the line-continuum ratio unreliable. Instead, the intensity ratio of the line He_{II}(4686Å) and He_I(5876Å) was used for the temperature measurements. The dependence of this ratio on the temperature is plotted in Figure 4.17. Typical photomultiplier
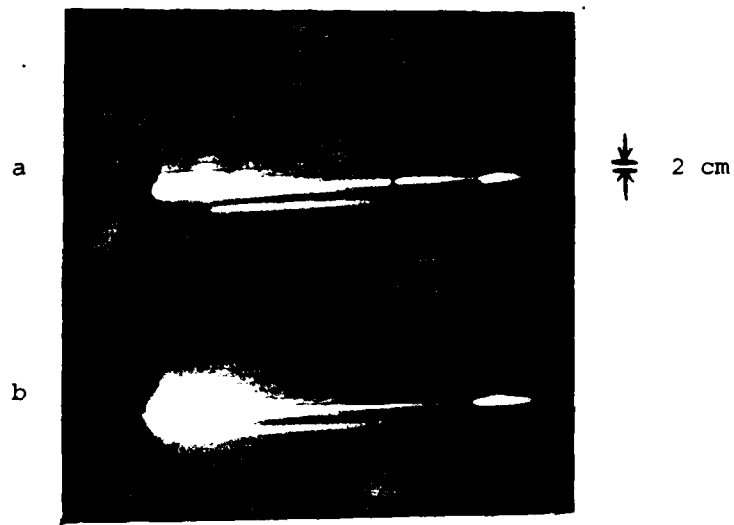
Figure 4.15.   Typical streak pictures of the beam

after the hole.

Total streak time = 10 μsec

a)   3 μsec delay   b)   4 μsec delay

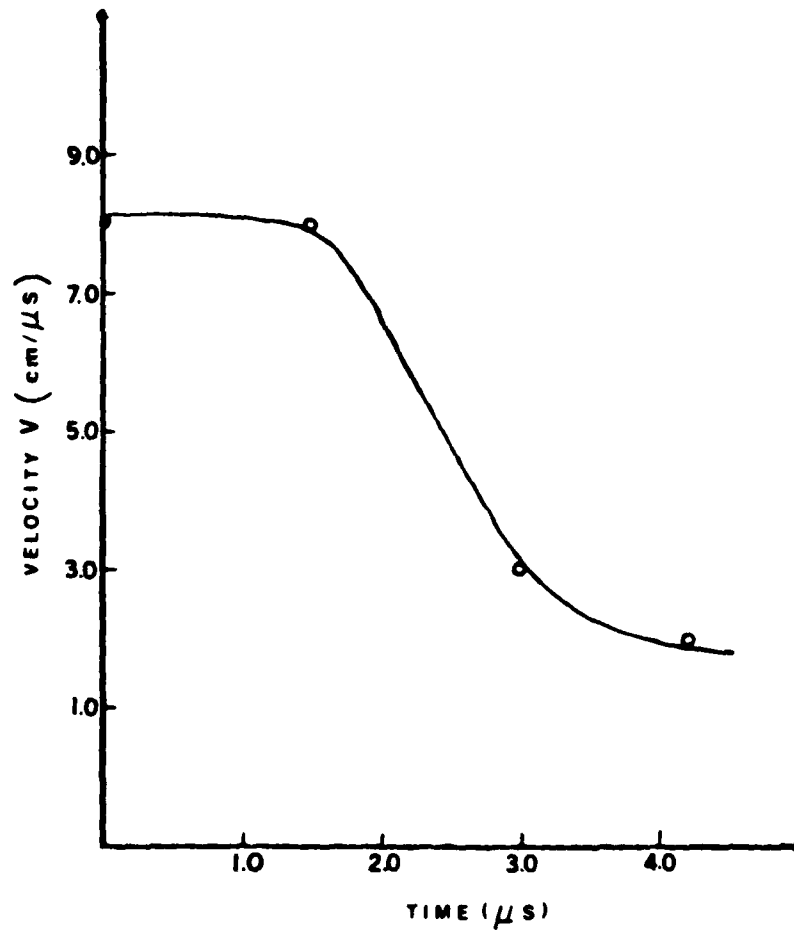V_G = 9 kV V_v = 8 kV   p = 2 psi

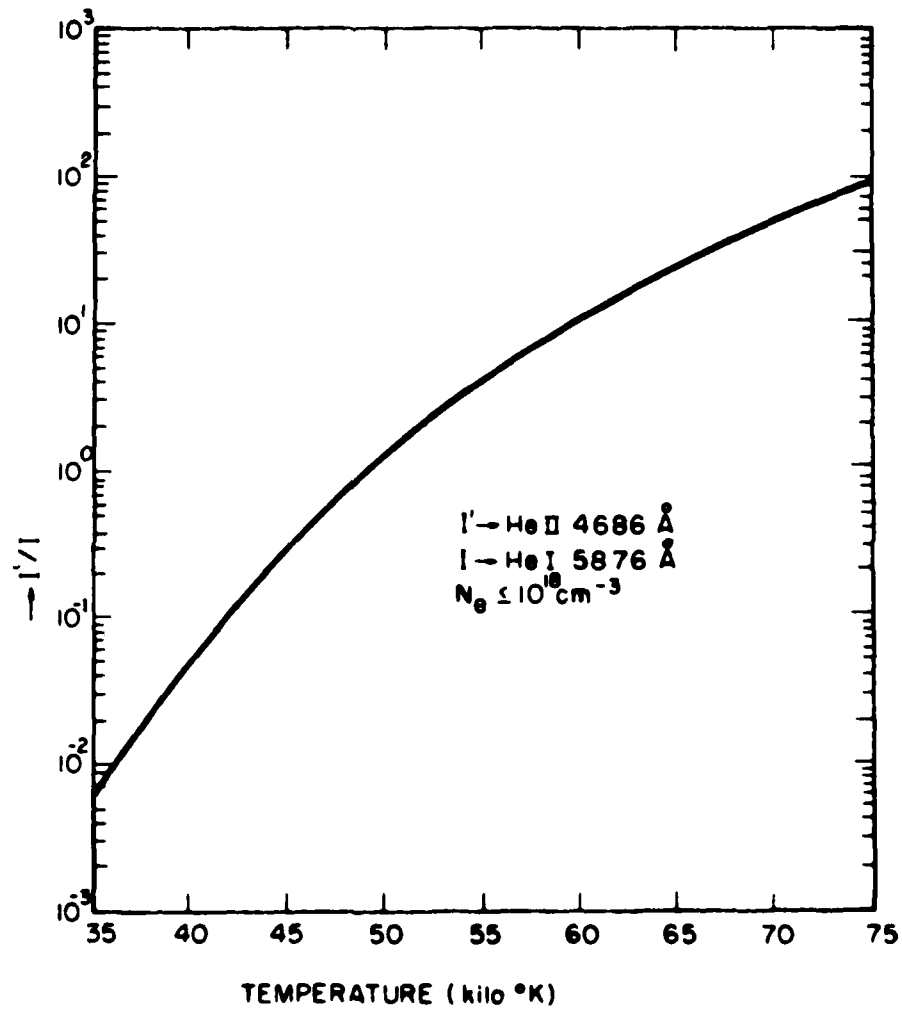Figure 4.16   Time variation of the beam velocity after

the hole.

Figure 4.17. Intensity Ratio of the Lines HeII 4686 Ang. and HeI 5876 Ang. as a Function of Temperature. (Ref. 26)

signals for the He_I and He_{II} lines before and after the hole are given
in Fig. 4.8b,c. Calculations indicated that the electron temperature
of the beam was lowered to 4 ± 0.4 eV by the presence of the plate.
Figure 4.18 gives a plot of the electron temperature of the plasma
jet at different distances away from the orifice and at different
times, indicating the consistency of the measurements.

Although the incident velocity was not evaluated, it is reason-
able to expect that since the temperature remained constant during
the beam-hole interaction, so would the velocity of the beam. The
computation of the initial Mach number M thus became straightforward
and gave $M = 4 \pm 0.4$.

The framing pictures (Figure 4.19) showing the beam-hole inter-
action revealed that the plasma stagnates as it impinges upon the
plate and escapes with a definite expanding angle rather than filling
in the volume behind the plate. The stagnation of the plasma pro-
vides further verification of the fluid approximation, while the
diverging structure of the jet verifies the compressibility assump-
tion of the fluid. In fact, the framing picture (Figure 4.20) of the
issuing jet taken during the earliest development of the escape gives
the escaping flow angle $\theta_2 \sim 34°$.

The framing pictures cited above were taken with the tungsten
slit.

For $M = (4 \pm 0.4)$, the theoretical curve of Figure 2.8 gives
$12 \le \theta_1 \le 15°$ and $35° \le \theta_2 \le 43°$.
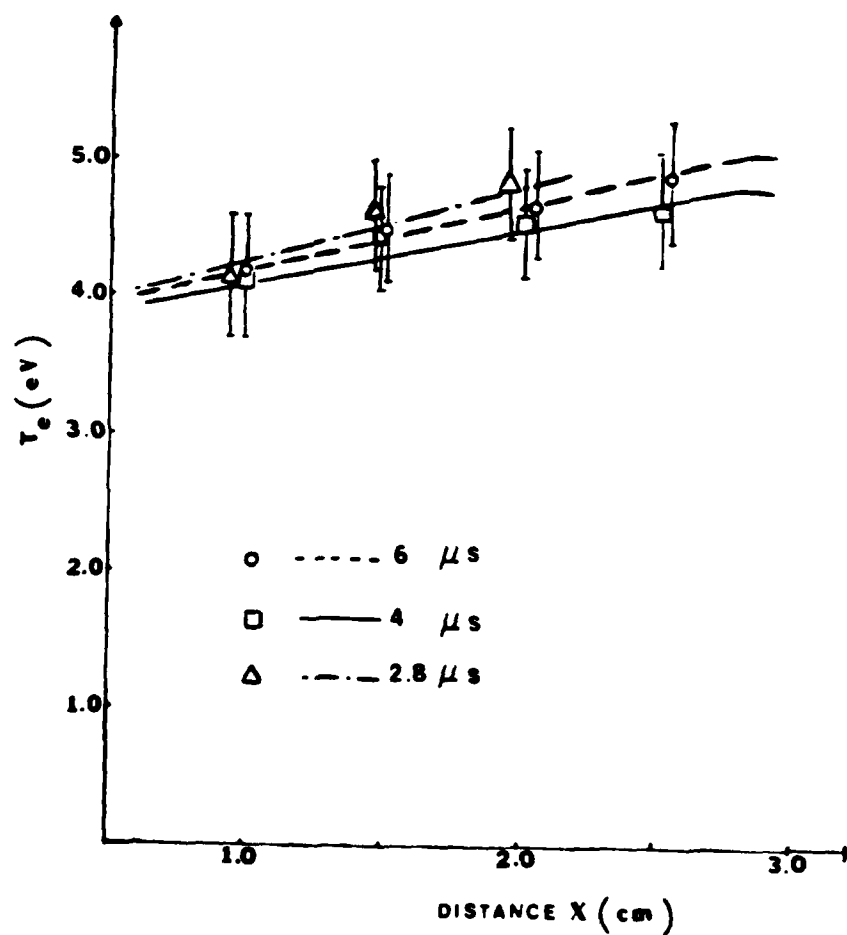
Figure 4.18. Electron temperature after the hole at different distances from the plate.
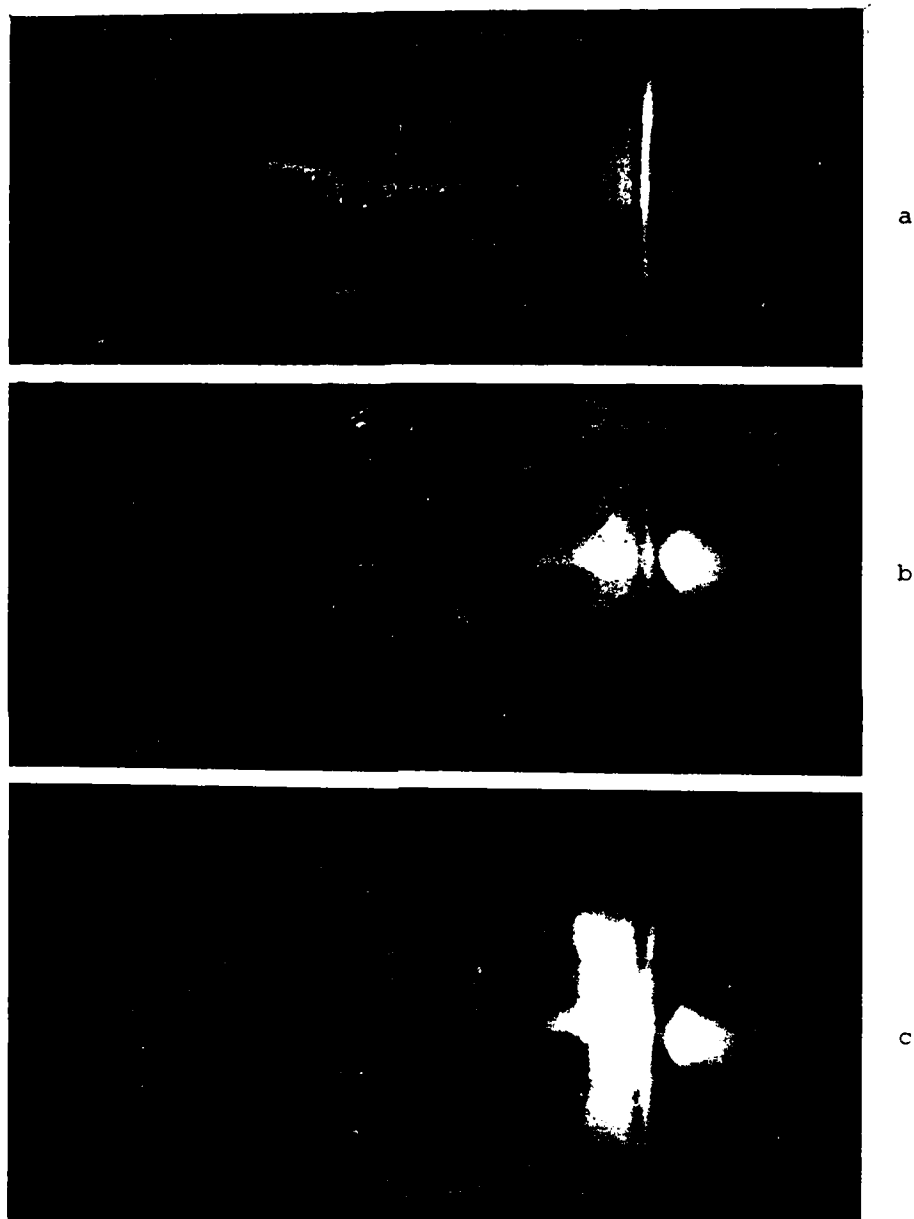
Figure 4.19. Framing pictures of the beam interaction with the tungsten slit. (50 nsec exposure).

$$\begin{matrix} \text{a. 1 } \mu\text{sec.} \\ \text{b. 2 } \mu\text{sec.} \\ \text{c. 2 } \mu\text{sec.} \end{matrix} \qquad \begin{bmatrix} V_G = 9 \text{ kV} \\ V_v^G = 8 \text{ kV} \\ p^v = 2 \text{ psi.} \end{bmatrix}$$

Figure 4.20 Framing picture of the escaping jet taken

at 2 μsec. (50 nsec exposure). The plate

is to the left.

V_G = 9 kV V_v = 8 kV   p = 2 psi

CHAPTER V

CONCLUSION AND SUGGESTIONS FOR FURTHER INVESTIGATIONS

5.1   Summary of Observations

The salient features of the beam-plasma interaction study can
be summarized as follows.

1)   The assumption of a uniformly collimated beam incident
on the hole is corraborated by the framing pictures (Figure 4.1).

2)   The beam dimensions are much larger than the width of
the slit. This makes the one dimension analysis justified.

3)   The Debye length λ_D and the ion-electron mean free
path λ_{ei}[32,33] are both much smaller than the size of the slit.
Typical values are:

$$\lambda_D = 4.7 \times 10^{-6} \text{ cm} \quad \lambda_{ei} = 2.15 \times 10^{-4} \text{cm} \quad \text{at } N_e = 10^{17} \text{cm}^{-3} \text{ and}$$

$$T_e = 4 \text{ eV}$$

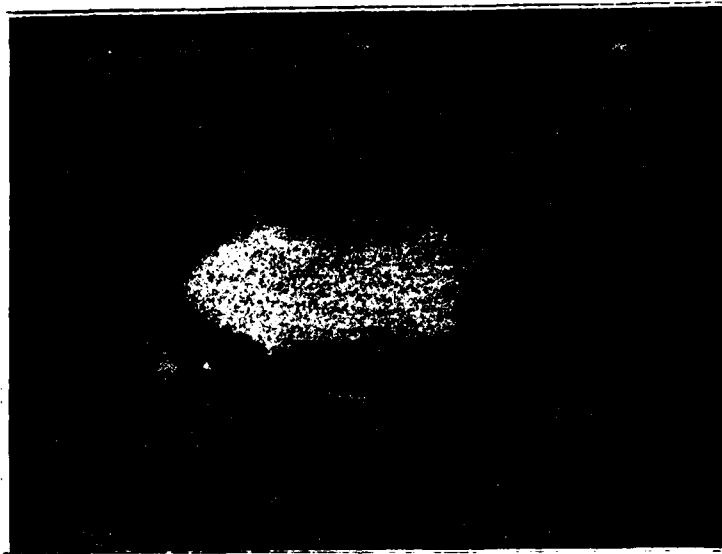$$\lambda_D = 1.49 \times 10^{-5} \text{cm} \quad \lambda_{ei} = 2.15 \times 10^{-2} \text{cm at } N_e = 10^{17} \text{cm}^{-3} \text{ and}$$

$$T_e = 40 \text{ eV}$$

4)   The plasma can be approximated by an inviscid fluid
model.

5)   The stagnation of the plasma at the plate surface is
consistent with our fluid theoretical approach.

6)   The steady state assumption is justified since the beam-
hole interaction time (< 1 μsec) is much shorter than the lifetime
of the beam (10 μsec) and the persistence time of the flow beyond the
hole.

7)   Various photographic data analyzing the emergence of the beam from the hole revealed that the plasma expands with a measurable angle as it comes out from the opening, thus indicating the assumed compressible character of the flowing plasma. An incompressible fluid would completely fill in the space.

8)   From the temperature and velocity measurements, one infers that the incident beam flow Mach number $M = 2$ is raised to $M = 4$ when the plate is present. These results show that the presence of the plate changes the character of the beam so as to cool the plasma considerably and at the same time reduce its velocity.

9)   The image converter camera pictures which provided an integrated light exposure over the whole Mach wave pattern, did not provide a check on the theoretical value of the initial flow angle θ_1 as a function of the Mach number M (Figure 2.9). These data, however, provided a means of finding experimentally the expanding flow angle θ_2 provided the measurements are made at the earliest stages of the jet development. The experimental values of θ_2 were slightly smaller than the theoretically predicted expanding angles. Since only visible light is recorded on the polaroid film, the fast cooling of the expanding plasma jet especially near the expansion angle θ_2 will not be recorded on the film, thus giving an experimental angle θ_2 less than the one predicted by the theory.

Framing pictures of the beam-hole interaction (Fig. 4.19) taken at latter stages in the development of the jet indicated large values

of θ_2 such as

$$\theta_2 = 65° \qquad \text{at} \quad 3 \text{ μsec}$$

$$\theta_2 = 71° \qquad \text{at} \quad 5 \text{ μsec}$$

This is explained by the fact that as the time goes on, the beam velocity after the hole decreases significantly as shown in Fig. 4.16, while the change in temperature is insignificant as illustrated in Fig. 4.18, thus causing the Mach number to decrease. This verifies the predicted behavior of θ_2 getting larger   for low Mach numbers as shown in Fig. 2.9.

10) The initial Mach number M may be changed by changing the initial beam velocity and temperature by varying the gun voltage and the back pressure. The relation between these different parameters are shown in Figures 4.3, 4.4, and 4.5. In particular, the angles θ_1 and θ_2 will thus be strongly affected by the initial Mach number as illustrated in Fig. 2.9.

5.2   Conclusion

As the jet travels away from the hole, the rise of the beam temperature with distance (Fig. 4.18) seems to contradict the theoretical predictions of the drop in temperature as shown in Figures 2.7 and 2.8. This slight rise of temperature may be attributed to weak shock wave formation after the hole, which cannot be detected with the image converter camera due to overshadowing of the original plasma light by the ablated material. Since initial shock wave formation

was excluded in the theoretical considerations, the formation of shock
wave is explained as follows. At the early stages of the jet escape,
the ratio between the exit pressure of the jet and the back pressure
of the outer medium is still very high (∞) causing the jet to expand
with a given diverging angle ($\theta_2 < 40°$). At later stages, due to the
slow evacuation of the vacuum chamber by the vacuum pumps, the back
pressure in the outer medium increases thus causing the exit to back
pressure ratio to become finite, leading to the possibility of
generating compression waves eventually leading to the formation of
shock waves on the escaping jet.

When the effects of more than one hole are considered, the
theoretical calculations carried out in Chapter 2 predicted a highly
mixed plasma region in the vicinity of the holes at low Mach numbers
(Fig. 2.11) mainly due to the large diverging angle θ_2. The extent
of the incident plasma parameters, i.e., density and temperature are
confined to a triangular region (Fig. 2.10), having large cone angles
for low Mach numbers. Therefore, a non-uniformity of the plasma
density is expected in both axial and azimuthal directions in the
implosion chamber. On the contrary, at high Mach numbers, very small
plasma mixing is expected to take place within the height of the
implosion chamber. However, in these cases, the incident plasma
state extends more into the implosion chamber. Finally, a continuity
of the incident plasma beam state emerges out of the holes forming
plasma bars at extremely large Mach numbers due to the presence of
the 90 holes.

Periodic azimuthal non-uniformity is therefore, expected for very large Mach numbers.

One recalls that in Chapter I the calculated minimum number density required for the necessary plasma injection has been determined from the ideal case of an infinite Mach number. From this discussion it appears that an optimum Mach number can be found that is needed to fulfill the requirements of the Shiva experiment, as far as the uniformity considerations are concerned.

For the Mach number $M \simeq 4$ used in the experiments, theoretical calculations predict that an initial plasma density N_e of the order of $\sim 2.43 \times 10^{17} cm^{-3}$ is necessary to assure at least a number density of $\sim 10^{17} cm^{-3}$ or more from each hole within a slab of 1 cm wide and 2 cm long. Thus, the plasma density produced by the gun operating at gun voltage ~ 11 kV, valve voltage ~ 8 kV and back pressure of ~ 2 psi fulfills the above criteria for minimum density in a Shiva implosion chamber.

Also, for Mach number 4 and an opening of 1 cm, the initial state extends to a distance $X_1 \simeq 3.87$ cm falling therefore beyond the length of the implosion chamber indicating that no reflection of the expansion Mach waves for the axial wall symmetry is expected. One notices that, if the separation between two neighboring holes is 1 cm, the plasma mixing occurs very close to the entry holes $X_2 \sim 0.6$ cm.

With the existing diagnostic equipment, due to high level of

optical radiation by the ablated materials, the spatial variations of
the plasma density after the hole were not measured.

Visual observations revealed that considerable amounts of elec-
trode material has been ablated from the hole region and transported
by the incident plasma beam into the implosion chamber. In fact, from
simple geometrical considerations, it was found that the ablatant
material, injected into the implosion chamber in addition to the
original He plasma, is evaluated to be 2 mgms (for Al) per shot.
This ablation phenomenon may change the concept of the plasma injec-
tion in the implosion chamber. With such high ablation from high Z
materials, the ablatants may thus provide more than the required mass
density for the implosion chamber, thus considerably relaxing the
injection criteria for a purely gaseous plasma.

5.3 Suggestions for Further Investigations

In order to fully understand the flow of a plasma beam through
a hole, further study is required both theoretically and experi-
mentally.

One of the main investigations will be to clarify in more
detail the formation, structure and dynamics of the beam ejected
from the coaxial gun. For this, some modifications have to be under-
taken on the gun in order to facilitate the experimental measurements
inside the barrel of the gun.

In the study of the beam-hole interaction itself a very impor-
tant parameter which needs to be measured experimentally is the

distribution of the magnetic field. The presence of the magnetic field and of electric currents flowing between the interaction plate and the gun will modify the fluid equations used in Chapter 2 as well as the dynamics of the beam formation in the gun.

In order to visualize the Mach wave pattern in detail, Schlieren photographic techniques[34] are recommended. The eventual existence of any shock wave at the escaping jet structure will be apparent by this technique.

Also spatial and temporal distribution of the temperature and density after the opening are important parameters to be monitored in order to fully analyze the escaping jet. To avoid a single shot type experiment, a sampling unit should be incorporated in the diagnostic equipment to evaluate line profile and continuum measurements simultaneously.

Another important further study will be the systematic investigations of the mechanism of the electrode material ablation. Specifically, the temporal and spatial characteristics of the ablatants are needed. A double holographic interferometry technique[35] using the line wings of the optical radiation from the ablatant materials is suggested for that purpose. For the evaluation of the amount of ablatants deposited on the second electrode, a thin film interferometry may be used.

Also, as pointed out in Chapter 2, for the plasma beam-hole interaction, cylindrical coordinates should be used in the theory

in order to obtain more realistic solutions to the injection problem.
Study should be focussed on a computer solution to carry out the
necessary iterations in the computations.

REFERENCES

1. William L. Baker and Norman F. Frederick, "Shiva Electromagnetic Implosion X-Ray Source", Tech. Report AFWL-TR-77-252 (1978) Kirtland Air Force Base, NM87117.

2. P. J. Turchi and W. L. Baker, J. Appl. Phys. 44, 4936 (1973).

3. W. J. Choce and H. K. Moore, Plenum Press, N. Y., 1968.

4. J. H. Degnan and R. E. Reinovsky "On Forming Cylindrical Gas Shells in Electrode Gaps for Electromagnetic Implosion Plasma Generation", Tech. Report AFWL-TR-75-265 (1976) Kirtland Air Force Base N19.

5. M. Wolfe, private communication. Wolfe unfortunately never had an opportunity to test his idea since he died in an accident.

6. A. M. Ferendeci et al., "Plasma Injection for a Shive Machine", Tech. Report 1978, Case Western Reserve University.

7. O. K. Mawardi, Proposal on the Coaxial Gun Injection of Plasma Shells into Shiva Implosion Chanbers, Case Western Reserve University, Cleveland, 1977.

8. O. K. Mawardi, Proceedings of an International Symposium on Plasma Guns, Phys. of Fluids, Vol. 7, No. 11, (Nov. 1964).

9. D. Y. Ching, Bull. Am. Phys. Soc. 13, 1560 (1968).

10. J. J. Lee, "Interaction of a Plasma Beam With a Magnetic Barrier," Technical Report A-65, Case Western Reserve University, 1973.

11. A. Gattozzi, "Study of a Collisionless Shock in a Plasma," Tech. Report A-70, Case Western Reserve University, 1974.

12. L. Howarth, "Modern Developments in Fluid Dynamics High Speed Flow", Vol. 1, Clarendon Press, 1956.

13. D. C. Pack, "On the Formation of Shock-waves Supersonic Gas Jets", Quart. J. Mech. Appl. Math. 1 (1948), 1.17.

14. G. S. Schmidt, "Physics of High Temperature Plasma", Academic Press, N. Y., 1966.

15. J. A. Owczarek, "Fundamentals of Gas Dynamics" International Textbook Co., Scranton, Pennsylvania, 1964.

16. James E. A. John, "Gas Dynamics", Allyn and Bacon, Boston, 1969.

17. M. J. Zucrow and J. A. Hoffman, "Gas Dynamics", Vol. 1 and 2, John Wiley & Sons, Inc., N. Y., 1976.

18. R. Courant and K. O. Friedrichs, "Supersonic Flow and Shock Waves," Interscience Publishers, Inc., N.Y., 1967.

19. A. H. Shapiro, "Compressible Fluid Flow", Vol. 1, Ronald Press Co., N. Y., 1953.

20. L. Fox, "Numerical Solution of Ordinary and Partial Differential Equations", Perganon Press, N. Y., 1962.

21. J. N. Mueller, "Equations, Tables and Figures for Use in the Analysis of Helium Flow at Supersonic and Hypersonic Speeds," National Advisory Committee for Aeronautics TN4063, Washington, Sept. 1957.

22. O. K. Mawardi, "Penetration of Plasma Beam in a Magnetic Barrier", Tech. Report AFCRL-71-0200 (1971), Case Western Reserve University.

23. C. E. Speck, J. J. Lee and O. K. Mawardi, Plasma Science, Vol. PS-5, No. 3, p. 151 (Sept. 1977).

24. D. E. T. Ashby, et al., J. Appl. Phys., 36, 29 (1965).

25. M. R. Null and W. W. Lozier, J. Optical Soc. of Am., 52, #10 pp. 1156-62 (Oct. 1962).

26. H. Griem, "Plasma Spectroscopy", McGraw-Hill Co., N. Y. 1964.

27. G. Bekefi, "Principles of Laser Plasmas," John Wiley & Sons, N.Y., 1976.

28. R. H. Huddlestone and Stanley L. Leonard, "Plasma Diagnostic Techniques", Academic Press, N. Y., 1965.

29. W. Lochte-Holtgreven, "Plasma Diagnostics", North-Holland Publishing Co., Amsterdam, 1968.

30. R. C. Elton, Stark Profile Measurement of the Lyman-α and Lyman-β Lines of Hydrogen, (U. S. Naval Research Laboratory No. 5967, July 17, 1963).

31. E. A. McLean and S. A. Samuel, Phys. Rev. 140, A1122, 1965.

32. Francis F. Chen "Introduction to Plasma Physics", Plenum Press, N. Y. and London, 1971.

33. B. S. Tanenbaum, "Plasma Physics", McGraw-Hill Book Co., New York, 1967.

34. B. E. Keen "Plasma Physics" Inst. of Physics, London and Briston (Conference Series #20), p. 160-161 (1974).

35. D. K. Koopman et al.,"Resonant Holography of Plasma Flow Phenomena", Rev. Sci. Instr., 49, 524 (April 1978).

SECURITY CLASSIFICATION OF THIS PAGE (When Data Entered)

REPORT DOCUMENTATION PAGE	READ INSTRUCTIONS BEFORE COMPLETING FORM

1. REPORT NUMBER	2. GOVT ACCESSION NO.	3. RECIPIENT'S CATALOG NUMBER
AFOSR-TR-79-1329		

4. TITLE (and Subtitle)
CHARACTERISTICS OF PLASMA-BEAM WALL INTERACTIONS

5. TYPE OF REPORT & PERIOD COVERED
FINAL REPORT,
Apr 1978 — Jun 79

6. PERFORMING ORG. REPORT NUMBER

7. AUTHOR(s)
O. K. MAWARDI, A. M. FERENDECI
R. MESLI

8. CONTRACT OR GRANT NUMBER(s)
AFOSR-78-3603

9. PERFORMING ORGANIZATION NAME AND ADDRESS
PLASMA RESEARCH LABORATORY
CASE WESTERN RESERVE UNIVERISTY
UNIVERSITY CIRCLE, CLEVELAND, OHIO 44106

10. PROGRAM ELEMENT, PROJECT, TASK AREA & WORK UNIT NUMBERS
2301/A2   61102F

11. CONTROLLING OFFICE NAME AND ADDRESS
AFOSR/NP
Bolling AFB, Bldg.#410
Wash DC 20332

12. REPORT DATE
30 Jun 79

13. NUMBER OF PAGES
76

14. MONITORING AGENCY NAME & ADDRESS(if different from Controlling Office)

15. SECURITY CLASS. (of this report)
UNCLASSIFIED

15a. DECLASSIFICATION DOWNGRADING SCHEDULE

16. DISTRIBUTION STATEMENT (of this Report)

Approved for public release;
distribution unlimited.

17. DISTRIBUTION STATEMENT (of the abstract entered in Block 20, if different from Report)

18. SUPPLEMENTARY NOTES

19. KEY WORDS (Continue on reverse side if necessary and identify by block number)

PLASMA BEAM
PLASMA INJECTION
DENSE PLASMAS
PLASMA BEAM - WALL INTERACTION

approx. =   times 10 to the 17th power/cu.cm.

20. ABSTRACT (Continue on reverse side if necessary and identify by block number)
Highly energetic ($\cong$ 42 eV) and dense ($\cong 4 \times 10^{17}$ cm^{-3}) plasma beams with directed velocities ($\cong$ 20 cm/μs) obtained by an improved version of a Cheng type coaxial gun have been directed towards a perforated metallic plate to study the beam-hole interaction. Micros
Various diagnostic techniques such as optical interferometry, high speed photography, optical spectroscopy, voltage and current measurements have been performed to characterize the incident plasma beam and determine its different parameters in various conditions with and without the perforated plate. over

DD FORM 1473

UNCLASSIFIED

A single fluid model using the method of characteristics has been chosen to study the features of the escaping flow.

The presence of the perforated plate reduced the velocities as well as the temperature significantly thus modifying the properties and structure of the diverging jet.

Observations provided evidence that a large amount of material has been ablated from the hole region and transported with the escaping jet.